

This is a repository copy of *The PARP inhibitor talazoparib synergizes with reovirus to induce cancer killing and tumour control in vivo in mouse models.*

White Rose Research Online URL for this paper:

<https://eprints.whiterose.ac.uk/id/eprint/230921/>

Version: Published Version

---

**Article:**

Kyula-Currie, Joan, Roulstone, Victoria, Wright, James et al. (23 more authors) (2025) The PARP inhibitor talazoparib synergizes with reovirus to induce cancer killing and tumour control in vivo in mouse models. *Nature Communications*. 6299. ISSN: 2041-1723

<https://doi.org/10.1038/s41467-025-61297-w>

---

**Reuse**

This article is distributed under the terms of the Creative Commons Attribution-NonCommercial-NoDerivs (CC BY-NC-ND) licence. This licence only allows you to download this work and share it with others as long as you credit the authors, but you can't change the article in any way or use it commercially. More information and the full terms of the licence here: <https://creativecommons.org/licenses/>

**Takedown**

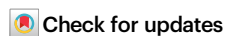
If you consider content in White Rose Research Online to be in breach of UK law, please notify us by emailing [eprints@whiterose.ac.uk](mailto:eprints@whiterose.ac.uk) including the URL of the record and the reason for the withdrawal request.


# The PARP inhibitor talazoparib synergizes with reovirus to induce cancer killing and tumour control in vivo in mouse models

Received: 18 March 2024

Accepted: 16 June 2025

Published online: 08 July 2025



Joan Kyula-Currie <sup>1,3</sup>✉, Victoria Roulstone <sup>1,3</sup>, James Wright <sup>1</sup>, Francesca Butera <sup>1</sup>, Arnaud Legrand <sup>1</sup>, Richard Elliott <sup>2</sup>, Martin McLaughlin<sup>1</sup>, Galabina Bozhanova<sup>1</sup>, Dragomir Krastev <sup>2</sup>, Stephen Pettitt <sup>2</sup>, Tencho Tenev<sup>1</sup>, Magnus Dillon <sup>1</sup>, Shane Foo <sup>1</sup>, Emmanuel C. Patin <sup>1</sup>, Victoria Jennings<sup>1</sup>, Charleen Chan Wah Hak <sup>1</sup>, Elizabeth Appleton <sup>1</sup>, Amarin Wongariyapak<sup>1</sup>, Malin Pedersen<sup>1</sup>, Antonio Rullan <sup>1</sup>, Jyoti Choudhary <sup>1</sup>, Chris Bakal <sup>1</sup>, Pascal Meier <sup>1</sup>, Christopher J. Lord <sup>2</sup>, Alan Melcher <sup>1</sup> & Kevin J. Harrington <sup>1</sup>

Reovirus type 3 Dearing (RT3D) is an oncolytic, double-stranded RNA virus. To identify potential RT3D drug-viral sensitizer, here we use a high-throughput screen of therapeutic agents and find a PARP-1 inhibitor, talazoparib, as a top hit. RT3D interacts with retinoic acid-induced gene-1 (RIG-I) and activates PARP-1, with consequent PARylation of components of the extrinsic apoptosis pathway. Pharmacological or genetic inhibition of PARP-1 abrogates this PARylation and enhances extrinsic apoptosis, NF- $\kappa$ B signalling and pro-inflammatory cell death. Interaction between PARP-1 and RIG-I induced by treating RT3D-infected cells with talazoparib activates downstream IFN- $\beta$  and TNF/TRAIL production to amplify the therapeutic effect through positive feedback. Furthermore, the effect of RT3D-talazoparib combination is phenocopied by non-viral ds-RNA therapy and RIG-I agonism. In vivo, mouse tumour model results show that RT3D/talazoparib combination regimen induces complete control of inoculated tumour as well as protection from subsequent tumour rechallenge with the, with accompanied innate and adaptive immune activation.

A number of oncolytic viruses are currently under development as potential anti-cancer therapies<sup>1–5</sup>. Drawn from a diverse range of viral species across the spectrum of RNA and DNA genomes, these agents have been extensively tested in wild-type, attenuated and engineered formats in both preclinical and clinical studies. Despite significant effort, the only therapy approved across multiple jurisdictions is a type I herpes simplex virus (HSV), talimogene laherparepvec (T-VEC), for use as a single-agent against melanoma<sup>3</sup>. There is a growing consensus that oncolytic viruses will only realise their full therapeutic potential as components of combination treatment regimens. As yet, attempts to

augment their efficacy and clinical relevance through combination with standard-of-care therapies, including surgery, chemotherapy, radiotherapy and immune checkpoint blockers have been largely unsuccessful<sup>6–13</sup> and have not led to new registrations or change of practice.

In the last two decades, following identification of the BRCA1 and 2 genes and elaboration of their role in homologous recombination (HR)-mediated DNA repair, poly(ADP)-ribose polymerase (PARP) inhibitors have been developed and approved as single-agent, synthetically lethal therapies in patients with HR-deficient breast, ovarian,

<sup>1</sup>The Institute of Cancer Research, London, UK. <sup>2</sup>The CRUK Gene Function Laboratory and Breast Cancer Now Toby Robins Research, London, UK. <sup>3</sup>These authors contributed equally: Joan Kyula-Currie, Victoria Roulstone. ✉e-mail: [joan.kyula@icr.ac.uk](mailto:joan.kyula@icr.ac.uk)

fallopian tube, peritoneal and prostate cancers<sup>14–18</sup>. All existing approvals for PARP1 and 2 inhibitors are predicated on tumours having germline or somatic mutations in components of DNA damage repair pathways and their use is based on specific testing for such abnormalities with companion diagnostic tests<sup>19</sup>. Attempts to combine PARP inhibitors with cytotoxic chemotherapy have been significantly complicated by overlapping, on-target toxicities<sup>20</sup>.

Previous studies have examined combinations of PARP inhibition with oncolytic HSV<sup>21</sup> or adenovirus<sup>22</sup>, with evidence of enhanced anti-tumour effects mediated by viral modulation of DNA repair processes. Such approaches have offered the prospect of inducing a state of PARP inhibitor sensitivity (or BRCAness), but they have not, as yet, translated effectively to clinical trials.

Here, we describe a novel biological interaction between PARP inhibition and the double-stranded (ds) RNA virus, reovirus type 3 Dearing (RT3D, pelareorep), that leads to synergistic anti-tumour activity that is independent of HR deficiency or modulation of DNA repair pathways. Instead, we demonstrate that PARP inhibition affects dsRNA sensing at the level of retinoic acid-inducible gene 1 (RIG-I) with consequent effects on extrinsic apoptosis, NF- $\kappa$ B signalling and pro-inflammatory cell death. Critically, we demonstrate that this effect can be phenocopied by non-viral ds-RNA therapy and RIG-I agonism, providing a clear line of sight to clinical translation of this therapeutic partnership with either viral or non-viral agents in tumour types beyond the relatively narrow confines of current licensed indications for PARP inhibition.

## Results

### RT3D combined with the clinical PARP inhibitor talazoparib exerts a robust synergistic effect in vitro and in vivo

We performed an unbiased, high-throughput small molecule screen in a 384-well plate format in A375 BRAF<sup>V600E</sup>-mutant melanoma cells to discover synergistic interactions between RT3D and 80 different small molecule inhibitors, approved or in late-stage development for cancer treatment (Supplementary Table 1). Talazoparib, (Lead therapeutic, Pfizer), an approved poly(ADP)-ribose polymerase 1/2 (PARP-1/2) inhibitor<sup>23</sup> caused profound sensitisation to RT3D in the high-throughput screen as highlighted in the red dots on the waterfall plot with values below  $-2$  being considered as a profound sensitisation effect (Fig. 1A and Supplementary Table 2A). Olaparib, another approved PARP-1/2 inhibitor was found to have a modest effect in terms of sensitisation to RT3D (Supplementary Table 2B) compared to talazoparib. This may be due to talazoparib being a more effective PARP inhibitor (and may also reflect its greater PARP trapping capabilities) as will be discussed later in the manuscript.

To validate our findings, RT3D plus talazoparib was tested on a panel of melanoma cell lines with different genetic backgrounds (BRAF mutant, RAS mutant and wild-type BRAF/RAS), to determine if virus-drug synergy persisted in multiple molecular contexts. Importantly, combination with talazoparib enhanced the effects of RT3D, regardless of the tumour cell line used, suggesting a robust synthetic lethal cytotoxic effect that remained irrespective of treatment schedule (Figs. 1C, S1, and S2A). This effect was significant and supra-additive when assessed by Bliss independence analysis (Fig. S2B). This effect is depicted for A375 and MeWo cell lines using the sulforhodamine B (SRB assay (Fig. 1B) and propidium iodide/Hoechst cell death assay with effects dependent on drug concentration and viral MOI (Fig. 1D, E). In addition, the effect of RT3D and talazoparib in triple negative breast cancer (TNBC) cell lines was assessed and a significantly enhanced effect was seen in the 4T1 (mouse) cell line as well as the SUM149 and Cal51 human cell lines. The SUM149 cell line, which harbours a BRCA1 mutation is known to be extremely sensitive to PARP1 inhibitors and, therefore, required a much lower concentration of talazoparib compared to the other cell lines (Fig. S2C).

To assess the wider potential of a RT3D/talazoparib combination in an in vivo setting, CD1 nude mice bearing A375 tumours were treated with vehicle, 0.1 mg/kg talazoparib,  $1 \times 10^6$  pfu RT3D or the combination [RT3D/talazoparib]. RT3D plus talazoparib significantly attenuated tumour growth (Fig. 1F) and prolonged survival (Fig. 1G) compared to either the vehicle, talazoparib or RT3D alone. Individual tumour volumes ( $n$  of 10) per treatment cohort are summarised (Fig. S3).

### Synergistic activity of RT3D plus talazoparib and its effects on DNA damage repair

Nuclear PARP-1 has a role in DNA damage repair (DDR) and the DDR pathway has previously been implicated in the effects of combining PARP inhibitors and oncolytic viruses<sup>21,22</sup>. Therefore, we examined the potential role of DDR pathways in mediating synergy between RT3D and talazoparib. First, cell cycle analysis revealed single-agent talazoparib caused a modest increase of cells at G<sub>2</sub>/M, consistent with the DNA damage expected from PARP inhibition. In contrast, RT3D infection increased the fraction of cells in S phase. Combination of RT3D and talazoparib caused a marked increase in the sub-G1 phase, which is indicative of apoptosis and consistent with the enhanced cell killing observed following RT3D/talazoparib (Fig. S4A).

Talazoparib, but not RT3D, induced markers of DNA damage and repair proteins  $\gamma$ H2AX and 53BP1 foci in A375 and MeWo cells. The combination of RT3D and talazoparib did not enhance  $\gamma$ H2AX and 53BP1 any more than with talazoparib alone (Fig. S4B–E). Finally, an alkaline COMET assay confirmed no increase in DNA damage due to single-stranded breaks following combined RT3D-talazoparib treatment (Fig. S4F). Taken together, these data suggest that the addition of RT3D to talazoparib did not overtly increase the level of DNA damage and, thus, an alternative mechanism must explain the observed synthetic lethality between RT3D and PARP inhibition.

### RT3D/talazoparib enhanced cell death is not mediated by enhanced viral replication

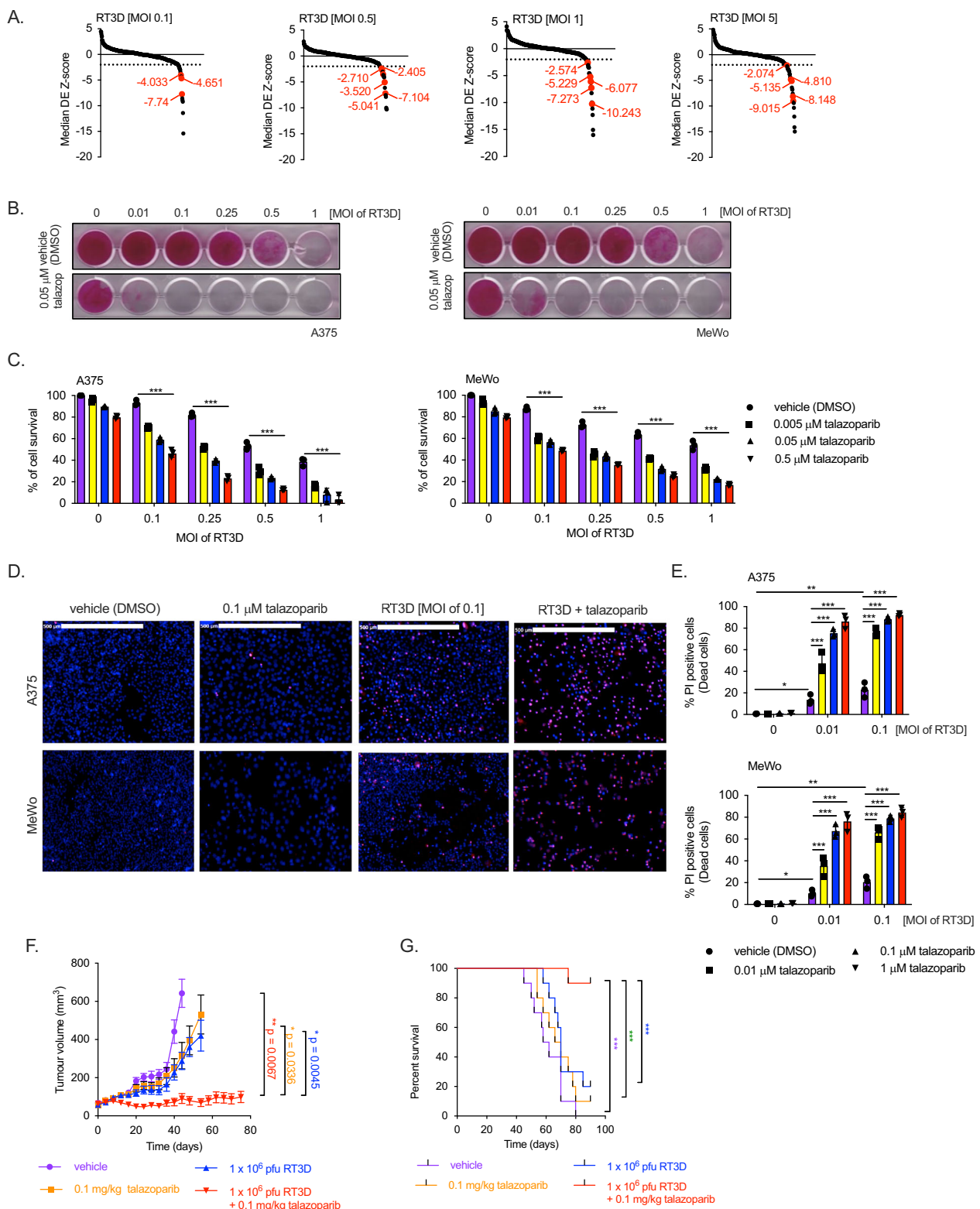
We next assessed whether increased viral replication could play a role in the RT3D-talazoparib synergistic effect. We measured viral replication in cells exposed to virus alone or the combination by one-step growth curve and viral plaque assays.

Addition of talazoparib to RT3D-infected cells did not result in any significant increase in production of intact, replication-competent RT3D in the one-step growth curve assays (Fig. S5A, B). Interestingly, although  $\mu$ 1C protein production was unaltered in all cell lines (in keeping with the one-step growth curve data), there was a modest increase in  $\sigma$ 3 production in A375 and MeWo, but not D04 cells (Fig. S5C). This observation is likely to reflect variations in the ability of RT3D to re-direct different cell lines to produce specific reoviral proteins. Nonetheless, taken together, these data clearly show that the combinatorial effect of talazoparib and RT3D cannot be explained in terms of increased viral replication (Fig. S5A, B).

### Loss of PARP-1 is synthetically lethal with RT3D

Previous studies have found that PARP-1 activation and PARylation of PARP-1-targeted proteins occurs when cells are infected with oncolytic HSV-1<sup>21</sup> and adenovirus (dl922-947)<sup>22</sup>. Similarly, we showed that RT3D infection leads to PARP-1 activation and PARylation across A375, MeWo and D04 cells. This effect was inhibited by talazoparib, as shown by both western analysis (Fig. 2A) and PAR ELISA (Fig. 2B) and was also manifested in vivo (Fig. 2C).

To further elucidate a potentially protective role of PARP-1 against RT3D-induced cell death, we assessed the effect of RT3D on isogenic HeLa cells with or without genetic ablation of the PARP-1 gene (PARP-1<sup>+/+</sup> wild-type cells or PARP-1<sup>-/-</sup> clones G3 and G9). PARP-1<sup>-/-</sup> clones were significantly more sensitive to RT3D (IC<sub>50</sub> MOI 0.1 and 0.05,



respectively) compared to their PARP-1<sup>+/+</sup> counterpart (IC<sub>50</sub> MOI > 10) (Fig. 2D).

As anticipated, PARP-1<sup>+/+</sup> cells showed enhanced cell kill when RT3D was combined with talazoparib. In contrast, in matched cells with genetic PARP-1 loss (G3 and G9), a high degree of sensitivity to RT3D infection alone was seen and this was not enhanced by the addition of talazoparib. Interestingly, the sensitivity of PARP-1<sup>-/-</sup> cells to RT3D alone was equivalent to that seen in wild-type PARP-1<sup>+/+</sup> cells

with the combination of RT3D and talazoparib (Fig. 2E, F). Similarly, A7 and F7 cells, which lack PARP-1 enzymatic function<sup>24</sup>, showed greater levels of sensitivity to RT3D that were not further increased with talazoparib treatment. Again, the sensitivity of A7 and F7 cells to RT3D alone appeared equivalent to that for wild-type PARP-1<sup>+/+</sup> cells treated with combined RT3D-talazoparib (Fig. 2G).

We also carried out gene silencing of PARP-1, PARP-2 or PARP-3 by siRNA in A375 cells to determine which PARPs were involved in



**Fig. 1 | RT3D combination with talazoparib exerts a synergistic effect. A** Results from a high-throughput screen experimental set up in the A375 melanoma cell line showing the RT3D multiplicity of infection [MOI] (ranging from 0.10 to 5) and a range of different drug inhibitors [ranging from 0.0005 [M-1] [M]. Cells were analysed 72 h post-infection using the Cell Titer Glo (CTG) Assay. The z score (DE effect z score = virus effect z score) is plotted on the Interestingly, although axis and was obtained from the standardised value from (i) the median of triplicate samples normalised to virus only versus untreated (ii) the mean of virus only versus untreated and (iii) the median absolute deviation between (i) and (ii) - also known as Z-MAD. The z score plots are shown for talazoparib in the presence of RT3D at MOI of 0.1, 0.5, 1 and 5 (highlighted in red dots) as displayed in the waterfall plots. **B** Cell survival was measured using the SRB assays following treatment with 0.05 [M of talazoparib and increasing doses of RT3D [0.01, 0.1, 0.25, 0.5 and 1] at 72 h post-infection. **C** A375 and MeWo cells were treated with increasing doses of talazoparib [0.005 [M, 0.05 [M or 0.5 [M] and thereafter infected with increasing doses of RT3D [MOI of 0.1, 0.25, 0.5 and 1]. Cell survival was assessed by MTT at 72 h post-infection. Data presented are mean values  $\pm$  SD,  $n = 3$  biologically independent experiments. P values were determined by two-way ANOVA corrected for multiple comparisons. **D** A cell death assay was used to measure the uptake of propidium

iodide (PI) following RT3D [MOI of 0.1] and talazoparib (0.1 [M] treatment at 48 h post-infection in A375 and MeWo cells. Representative pictures of cell death assay where dead cells are shown for PI uptake (red) and nuclear staining by Hoechst (blue). **E** Propidium iodide (PI) uptake following RT3D [MOI of 0.01 and 0.1] and talazoparib (0.01 [M, 0.1 [M or 1 [M] treatment at 48 h. Data presented are mean values  $\pm$  SD,  $n = 3$  biologically independent experiments. P values were determined by two-way ANOVA corrected for multiple comparisons. **F** CD1 nude mice carrying A375 tumour xenografts were treated with oral administration of vehicle (10% DMAC, 6% Solutol and 84% PBS) or 0.1 mg/kg talazoparib from Day 1–5. RT3D was injected intratumorally on Day 3 at  $1 \times 10^6$  pfu, or sham injection (PBS). Sizes of tumours were measured for each treatment cohort. Data presented are mean values  $\pm$  SEM and p values were determined by one-way ANOVA corrected for multiple comparisons. **G** Kaplan–Meier curve was evaluated for each treatment group to assess the median survival rate. There was significant prolongation of survival in the combination of RT3D and talazoparib compared to either agent alone ( $***p = 0.0003$  using a Log rank [Mantel-Cox] test). For (**F** and **G**), vehicle  $n = 10$ , RT3D  $n = 10$ , talazoparib  $n = 10$  and combination  $n = 10$  animals per group. P values were derived where \* = p value, \*\* = p value < 0.01 and \*\*\* = p value < 0.001. Source data are provided as a source data file.

regulating RT3D-induced PARylation. RT3D-induced PARylation persisted despite siRNA targeting PARP-2 and PARP-3, but not PARP-1 (Fig. S6A), as expected because PARP1 is the dominant PARP enzyme in cells. Additionally, resistance to RT3D, which could be overcome by talazoparib, persisted following treatment with siRNA against PARP-2 and PARP-3. In contrast, siRNA against PARP-1 completely phenocopied the cell kill observed by the RT3D-talazoparib combination (Fig. S6B–F). Taken together these data suggest PARP-1-induced PARylation confers resistance to RT3D, which can be counteracted by talazoparib.

### Proteome analysis using mass spectrometry to identify key pathways involved in regulating RT3D/talazoparib enhanced cell death

To further investigate the mechanistic interaction between RT3D and talazoparib, we analysed the proteome in a non-biased way by mass spectrometry. Briefly, we clustered the proteins into expression profiles across the four treatment groups (vehicle, 0.1  $\mu$ M talazoparib, RT3D [MOI of 0.1] or combination and then carried out pathway enrichment analysis on each cluster. Proteins were clustered into expression profiles across our treatment cohort groups: vehicle, 0.1  $\mu$ M talazoparib, RT3D [MOI of 0.1] or combination and then pathway enrichment analysis was carried out on each cluster. We identified the top three pathways that were enriched in clusters in which the highest expression was seen with combination treatment and the lowest expression in untreated cells, with the RT3D or talazoparib single-agent treatments showing intermediate expression, higher than untreated but lower than the combination treatment (Fig. 3A). Proteomic analyses following RT3D plus talazoparib highlight profound increases in the RIG-I (Fig. 3B), NF- $\kappa$ B (Fig. 3C) and apoptotic pathways associated with cell-surface death domains, in particular the death-inducing signalling complex (DISC), which includes Caspase-8 and RIPK1 (Fig. 3D).

In addition, we analyzed our data using STRING and a summary of significant proteins following RT3D/talazoparib treatment is highlighted as a graphical abstract (Fig. 3E). Briefly, we focused on proteins upregulated by RT3D compared to vehicle. Thereafter, we looked at proteins that were even further upregulated by the addition of talazoparib to RT3D (combination). We then built a network using STRING based on high-confidence molecular interactions and clustered them by using the MCL algorithm.

The remainder of this report focuses on these 3 key pathways and dissects the mechanisms through which they play a role in enhancing RT3D/talazoparib-induced cell death.

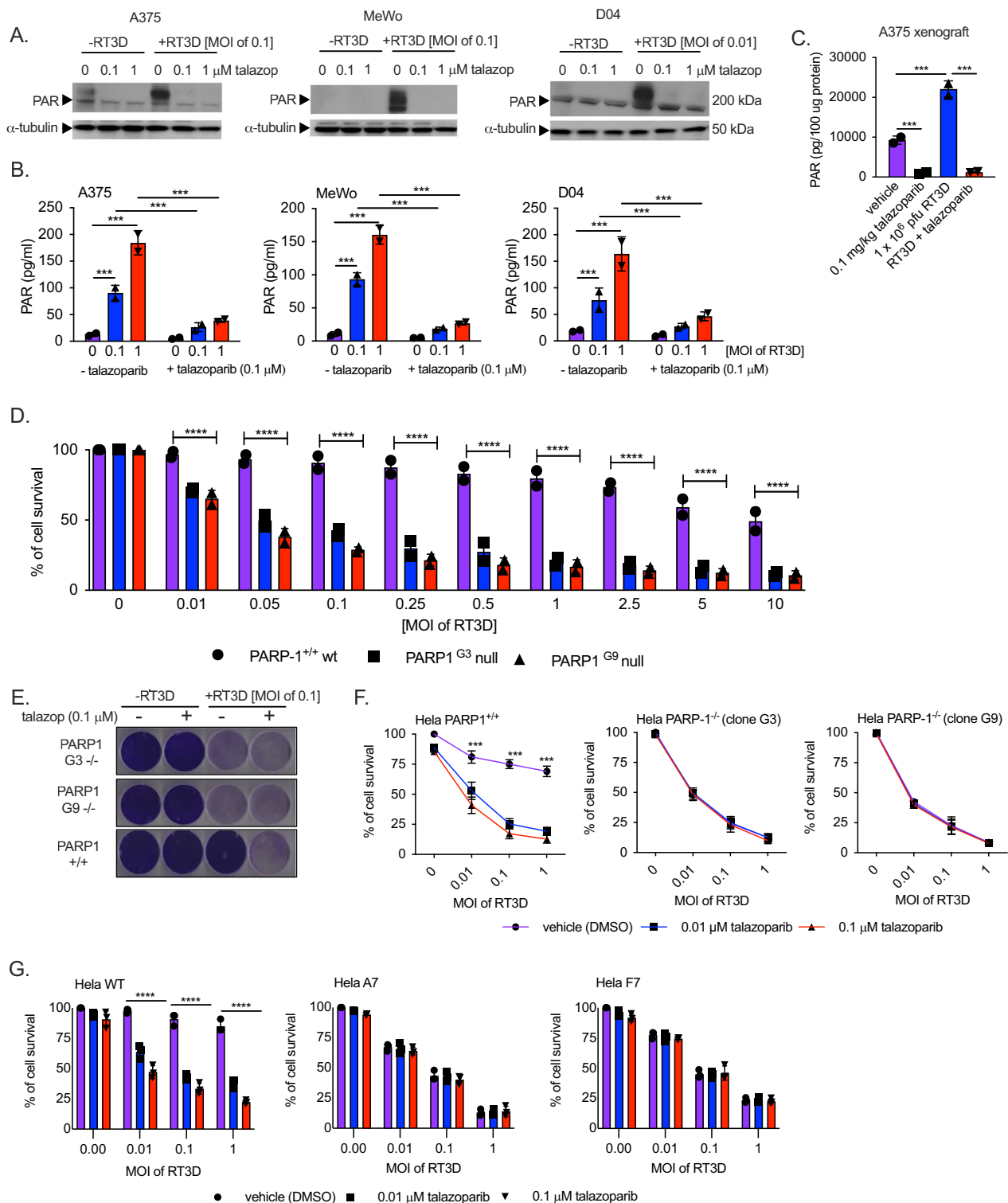
### PARP-1 regulates PARylation induced by RT3D infection and enhances death-inducing signalling complex (DISC)-mediated apoptosis

RT3D has previously been reported to induce apoptosis<sup>25–27</sup>. To probe the mechanisms of cell death, a caspase inhibitor screen was used to identify key caspases involved in RT3D plus talazoparib-mediated cell death. Caspase-8 rescued A375 and MeWo cells from RT3D-talazoparib-induced cell death to a greater extent than other caspase inhibitors (Fig. 4A). Western blotting confirmed Caspase-8 cleavage in response to RT3D-talazoparib across A375, MeWo and D04 cell lines. Caspase-8 cleavage correlated with caspase-3 and PARP cleavage (Fig. 4B). We next investigated this effect in vivo. Western blot analysis of A375 tumours revealed basal and RT3D-induced PARylation was inhibited by talazoparib, as expected. In accord with in vitro studies, RT3D-talazoparib combination resulted in increased levels of apoptosis as measured by cleaved PARP, Caspase-8 and -3 in the tumour (Fig. 4C). In isogenic (PARP-1<sup>+/+</sup>/PARP-1<sup>-/-</sup>) HeLa cells, an increase in PARylation following RT3D infection in PARP-1<sup>+/+</sup>, but not PARP-1<sup>-/-</sup> cells, was observed as expected. The RT3D-induced increase in PARylation in PARP-1<sup>+/+</sup> cells correlated with resistance to apoptotic cell death, as shown by absence of caspase-8 and caspase-3 cleavage. In contrast, cleaved caspase-8 and caspase-3 were observed in PARP-1<sup>-/-</sup> cells in response to RT3D (Fig. 4D). Furthermore, this effect in the PARP-1<sup>-/-</sup> cells could be phenocopied in PARP-1<sup>+/+</sup> cells by the addition of talazoparib (Fig. 4E).

Subsequently, we silenced components of the DISC, including Caspase-8, RIPK1 and FADD, by siRNA in A375 cells. These conditions protected cells against the combined effect of RT3D plus talazoparib (Fig. 4F, G). By western blot analysis, RT3D-induced PARylation was not affected by Caspase-8, RIPK1 or FADD siRNA, demonstrating that it occurred upstream of DISC activation (Fig. 4H). Conversely, PARP cleavage, as a marker of apoptosis, was prevented by transfection with Caspase-8, RIPK1 and FADD siRNA, implying that the DISC components play an important role in regulating combined RT3D-talazoparib-induced cell death.

### Talazoparib inhibits RT3D-induced poly(ADP)-ribose interaction with the DISC

Having shown that combined RT3D-talazoparib enhanced apoptosis mediated by the DISC, we explored the possibility of an interaction between DISC components and poly(ADP)-ribose (PAR) chains following RT3D infection. Firstly, we carried out an immunoprecipitation assay to pull down PAR, where PAR antibody was added to lysates in the presence of protein G-agarose beads and cleared lysates run by



Western analysis. Our data revealed PAR interaction with Caspase-8 (as well as FADD, TRADD and RIPK1) at 36 h. These interactions were reduced by talazoparib (Fig. 4I). Input protein analysis confirmed that RT3D-induced PARylation was inhibited by talazoparib (Fig. S7A).

Conversely, we carried out a second experiment where we pulled-down caspase-8 using the Complex II immunoprecipitation assay as detailed in the “Methods” section. Our results revealed an interaction between Caspase 8 and PAR (by 36 h) that, again, was attenuated in the presence of talazoparib (Fig. 4J). The interaction of DISC components, RIPK1 and FADD, with caspase-8 was also inhibited by talazoparib and

this correlated with an increase in cleaved caspase-8 as shown in the input data (Fig. S7B). Taken together, these data suggest that RT3D induces PARylation of DISC components to inhibit apoptosis, and that this effect is reversed by talazoparib, leading to enhanced cell death.

### RT3D plus talazoparib-induced cell death is mediated by TRAIL and TNF

TRAIL and TNF secretion activate DISC components through TRAIL receptors (DR4) and (DR5) or TNF receptors (TNFR1) and (TNFR2), respectively<sup>28,29</sup>. RT-PCR data showed RT3D-induced increases in both

**Fig. 2 | RT3D-induced PARylation is inhibited by talazoparib.** **A** A375, MeWo and D04 melanoma cells were pre-treated with 0.1  $\mu$ M talazoparib and thereafter infected with RT3D [MOI of 0.1 and 1]. Cells were harvested, and the lysates collected at 48 h post-infection. Poly ADP ribosylation (PAR) was assessed by immunoblotting. **B** PAR was also assessed by ELISA. Data presented are mean values  $\pm$  SD,  $n = 2$  biologically independent experiments.  $P$  values were determined by two-way ANOVA corrected for multiple comparisons. **C** CD1 nude mice bearing A375 tumour xenografts were treated with oral administration of vehicle (10% DMAC, 6% Solutol and 84% PBS) or 0.1 mg/kg talazoparib from Day 1–5. RT3D was injected intratumorally on Day 3 at  $1 \times 10^6$  pfu, or vehicle (10% DMAC, 6% Solutol and 84% PBS). Following the last treatment on day 5, tumours were harvested and assessed for PAR by ELISA. Data presented are mean values  $\pm$  SD,  $n = 2$  mice.  $P$  values were determined by one-way ANOVA corrected for multiple comparisons. **D** RT3D sensitivity was assessed in HeLa PARP-1 paired cells: PARP-1<sup>+/+</sup> (wild type) and PARP-1<sup>-/-</sup>

(clones G3 and G9), where cytotoxicity was measured by MTT assay 72 h post-infection. Data presented are mean values  $\pm$  SD,  $n = 2$  biologically independent experiments.  $P$  values were determined by two-way ANOVA corrected for multiple comparisons. **E** Cell viability assays were carried out to assess RT3D plus talazoparib in HeLa PARP-1 paired models (PARP-1<sup>+/+</sup> and PARP-1<sup>-/-</sup>) as shown by crystal violet assays. **F** SRB cell viability assay to assess RT3D plus talazoparib in HeLa PARP-1 paired models at 72 h post-infection. Data presented are mean values  $\pm$  SD,  $n = 3$  biologically independent experiments. **G** SRB cell viability assay to assess RT3D plus talazoparib in HeLa PARP-1 mutant models (A7 & F7) versus wild type. Data presented are mean values  $\pm$  SD,  $n = 3$  biologically independent experiments.  $P$  values were determined by two-way ANOVA corrected for multiple comparisons.  $P$  values were derived where \* =  $p$  value, \*\* =  $p$  value < 0.01 and \*\*\* =  $p$  value < 0.001. Source data are provided as a source data file.

DR4/DR5 (Fig. S8A) and TNFR1/TNFR2 expression (Fig. S8B) in A375 cells (that were unaltered with talazoparib treatment). RT3D induced TRAIL and TNF, measured by ELISA, the effects of which were counteracted by anti-TRAIL (2E5) (Fig. S8C) or anti-TNF neutralising antibodies, respectively (D1B4) (Fig. S8D). Cell death induced by RT3D or combination of RT3D and talazoparib was partially rescued by 2E5-mediated TRAIL (Fig. S8E) or TNF (Fig. S8F) neutralisation. In contrast to blocking TRAIL or TNF, activating TRAIL or TNF using soluble TRAIL (Fig. S8G) or TNF (Fig. S8H) ligand in combination with talazoparib showed a significant synergistic effect in A375 cells, and this phenocopied the cell death effect seen between RT3D and talazoparib. Like RT3D, TRAIL and TNF ligand induced PARylation, and this was lost following talazoparib treatment (Fig. S8I, J), respectively.

#### NF- $\kappa$ B activity and pro-inflammatory cytokine production is enhanced following RT3D and talazoparib treatment

To evaluate the immunogenic consequences of this combination therapy, a human cytokine array was carried out in A375 cells following RT3D plus talazoparib treatment. The pro-inflammatory cytokines CCL5, CXCL8, CXCL1 and CXCL10 were upregulated (Fig. 5A). Next, we evaluated the dependency of these cytokines on DISC components. Silencing of caspase-8, RIPK1 and FADD significantly reduced cytokines demonstrating the importance of the DISC in regulating cytokine production (Fig. 5B). These results correlated with previous data showing that TRAIL-induced cytokine production is regulated through FADD, RIPK1 and Caspase 8<sup>30</sup>.

We performed an ELISA-based assay that specifically detected increased DNA binding activity of the NF- $\kappa$ B p65 transcription factor RELA (p65) in nuclear extracts from cells treated with RT3D plus talazoparib compared to single-agent counterparts, in A375 and MeWo cells (Fig. 5C). To further understand how RT3D plus talazoparib affects NF- $\kappa$ B activity at the single-cell level, we tagged RELA with GFP and PCNA with Scarlet at endogenous loci in A375 cells using CRISPR-CAS9 to visualise changes in subcellular localisation of RELA by microscopy, using PCNA as a nuclear marker (Fig. 5D)<sup>31</sup>. Cells were imaged by confocal microscopy and single cells tracked using automated image analysis. Nuclear RELA was calculated for each timepoint. The proportion of RELA-responsive cells was highest with RT3D plus talazoparib relative to single-agent counterparts and correlated with the highest percentage of tracked cells dying during the 48-h imaging period (Fig. 5E, F). Figure 5G shows an exemplar cell being tracked following RT3D plus talazoparib treatment where high RELA nuclear localisation was noted around 36 h prior to cell death, which happened before 48 h.

We further assessed the combinational effects of RT3D and PARP inhibition on cell death and NF- $\kappa$ B signalling using the alternative PARP inhibitors, olaparib and veliparib. RT3D increased NF- $\kappa$ B activity with talazoparib at lower doses when compared with olaparib or veliparib (Fig. S9A). Cell viability analysis by crystal violet staining showed that, like talazoparib, olaparib increased RT3D-induced cell death, while

veliparib had modest effects on cell viability (Fig. S9C). In addition, the cytokines CCL5, CXCL1 and CXCL10 induced by RT3D was increased with talazoparib at 1  $\mu$ M, but not with olaparib and veliparib at 1  $\mu$ M (Fig. S9B). Additionally, we found either talazoparib or olaparib in combination with RT3D led to a greater increase in apoptotic markers (caspase-8, caspase-3 and PARP cleavage) when compared to RT3D alone, which was not seen with veliparib (Fig. S9D). However, olaparib was used at a far higher dose (10  $\mu$ M) than talazoparib (0.1  $\mu$ M). We found a higher dose of veliparib 20–25  $\mu$ M was necessary to see an effect similar effect as that seen with olaparib at lower doses of 5–10  $\mu$ M (Fig. S9E).

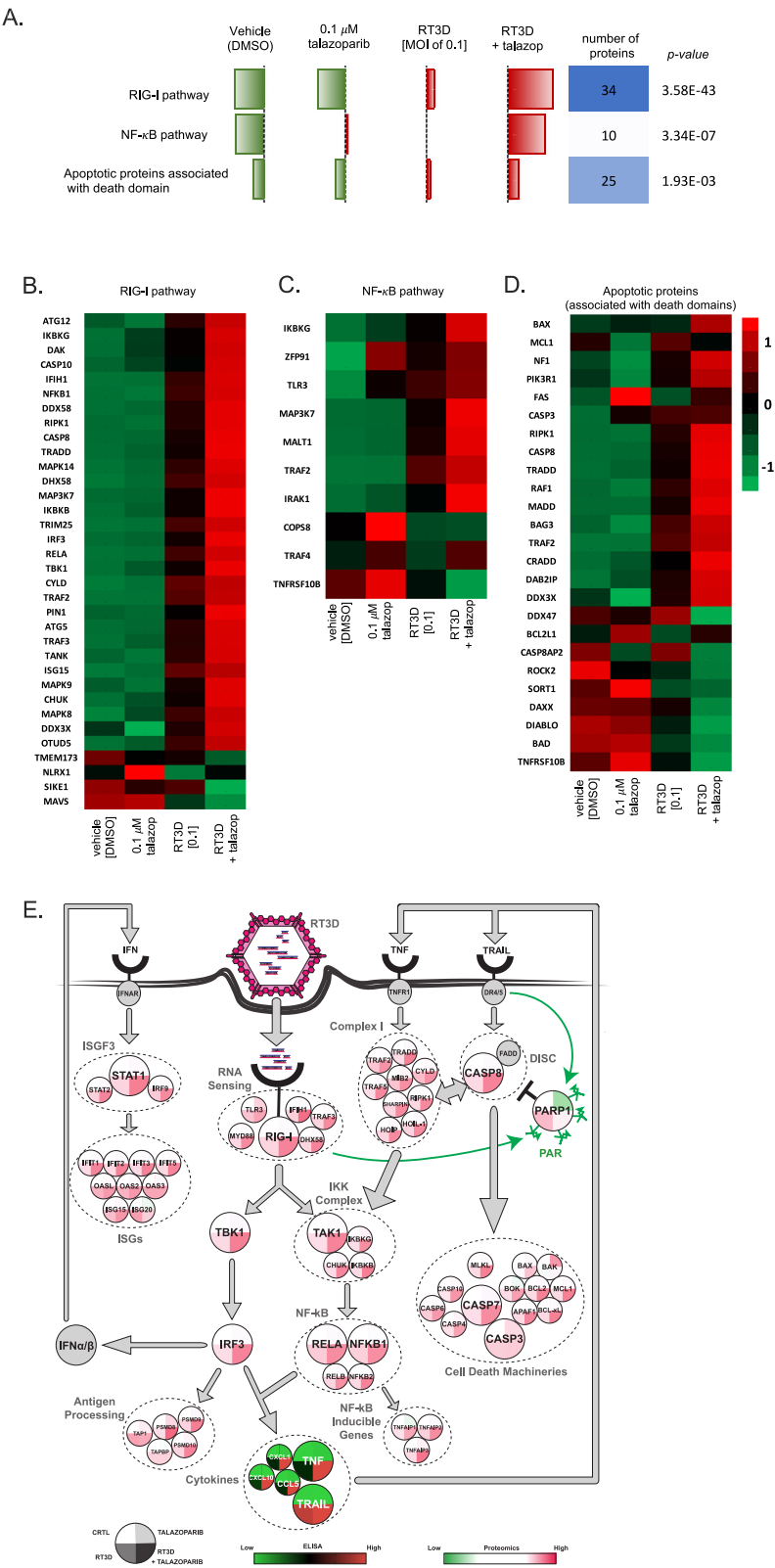
To address whether the cytokines upregulated by RT3D plus talazoparib are NF- $\kappa$ B-regulated, we used the I $\kappa$ B $\alpha$  inhibitor, BAY11-7082, which is widely used as an inhibitor of downstream NF- $\kappa$ B. RT3D plus talazoparib-induced cytokine production of CCL5, CXCL8, CXCL1 and CXCL10 was significantly reduced by BAY 11-7082, highlighting the importance of NF- $\kappa$ B in regulating these cytokines (Fig. 5H).

Finally, to assess the link between p65 NF- $\kappa$ B activity and the DISC complex, the DNA binding activity of NF- $\kappa$ B was measured in A375 cells after gene silencing of caspase-8, RIPK1 and FADD. NF- $\kappa$ B activity induced by RT3D or RT3D plus talazoparib was abrogated after siRNA of each DISC component (Fig. S10A). Furthermore, NF- $\kappa$ B activity in A375 cells was significantly reduced by co-treatment with neutralising TRAIL antibody (2E5) or neutralising TNF $\alpha$  antibody (D1B4) demonstrating a possible link between TRAIL or TNF $\alpha$  and NF- $\kappa$ B signalling (Fig. S10B) following RT3D plus talazoparib treatment. Collectively, these data suggest that PARP-1 regulates TRAIL-mediated cell death caused by RT3D infection and that this protective effect of PARP-1 can be pharmacologically modulated to elicit enhanced cell death through signalling via DISC and NF- $\kappa$ B pathways.

#### Talazoparib enhances the IFN- $\beta$ signalling pathway through RIG-I

Subsequently, we explored events upstream of NF- $\kappa$ B signalling. Pattern recognition receptors (PRRs) such as the RNA helicase, RIG-I, trigger activation of transcription factors NF- $\kappa$ B and IRF3. Indeed, proteomic analysis showed a profound increase in the RIG-I pathway (Fig. 3), and this was further confirmed by western analysis where RIG-I, phosphorylated STAT-1 and phosphorylated IRF-3 were all increased following RT3D plus talazoparib treatment compared to either agent alone (also correlating with a loss of RT3D-induced PARylation) (Fig. 6A). The effect of RIG-I signalling on RT3D plus talazoparib-induced cell kill was assessed by silencing RIG-I. This showed that RIG-I siRNA partially rescued enhanced cell kill following RT3D plus talazoparib treatment (Fig. 6B). This was confirmed further by western analysis which showed abrogation of PARP cleavage with RIG-I siRNA (Fig. 6C). Moreover, RT3D plus talazoparib-induced IFN- $\beta$  secretion was significantly reduced following RIG-I silencing (Fig. 6D).

Given the important role of RIG-I in RT3D plus talazoparib-mediated cell death, we tested whether apoptosis induced by RT3D



plus talazoparib combination treatment was virus-dependent or whether this effect could also be driven by non-viral RNA sensor agonism. In place of RT3D, we used RNA tool compounds, poly I:C (synthetic dsRNA) and 3p-hRNA (a RIG-I agonist), in combination with talazoparib. Both compounds induced PARylation and phenocopied the effect of RT3D-talazoparib (Fig. S11A). Talazoparib inhibited PARylation induced by these tool compounds and that correlated with

increased PAR-cleavage (Fig. S11A), IFN- $\beta$  production (Fig. S11B) and cell death as shown by crystal violet and SRB assays, respectively (Fig. S11C, D). Given our findings that RNA sensor agonists can trigger PARylation, and since PARP-1 has nucleic acid binding capabilities, we investigated whether PARP-1 interacts directly with RNA sensors, such as RIG-I, using a PARP-1-Trap agarose assay. Our data demonstrated an



**Fig. 3 | Proteins were clustered into expression profiles across our treatment cohort groups: vehicle, 0.1  $\mu$ M talazoparib, RT3D [MOI of 0.1] or combination (RT3D/talazoparib) and then pathway enrichment analysis was carried out on each cluster. Three key pathways: RIG-I, NF- $\kappa$ B and apoptotic proteins (associated with death domains) were found to be enriched in the cluster where highest expression was with combination treatment (RT3D/talazoparib) compared to 0.1  $\mu$ M talazoparib or RT3D [MOI of 0.1] which showed higher expression than vehicle (A). The proteins expressed in the key pathways are summarised as heatmaps with the RIG-I pathway (B), NF- $\kappa$ B pathway (C) and apoptotic proteins [associated with death domains] (D). Graphical abstract summarising the relevant proteins involved**

in the recognition, signalling and execution of RT3D infection and talazoparib treatment following STRING analysis (E). Each protein is represented by a circle divided in four parts: vehicle, 0.1  $\mu$ M talazoparib, RT3D [MOI of 0.1] or combination (RT3D/talazoparib). These levels are color-coded from green (low expression) to white (identical expression) to red (high expression) and represent their value normalised to vehicle. In addition, cytokines that were analysed by ELISA are summarised (*as detailed in Fig. 5B and Supp Fig. 8*). RIGI-PARP1 interaction studies are summarised later in the paper (Fig. 6E and Supp Fig. 11E). Source data are provided as a source data file.

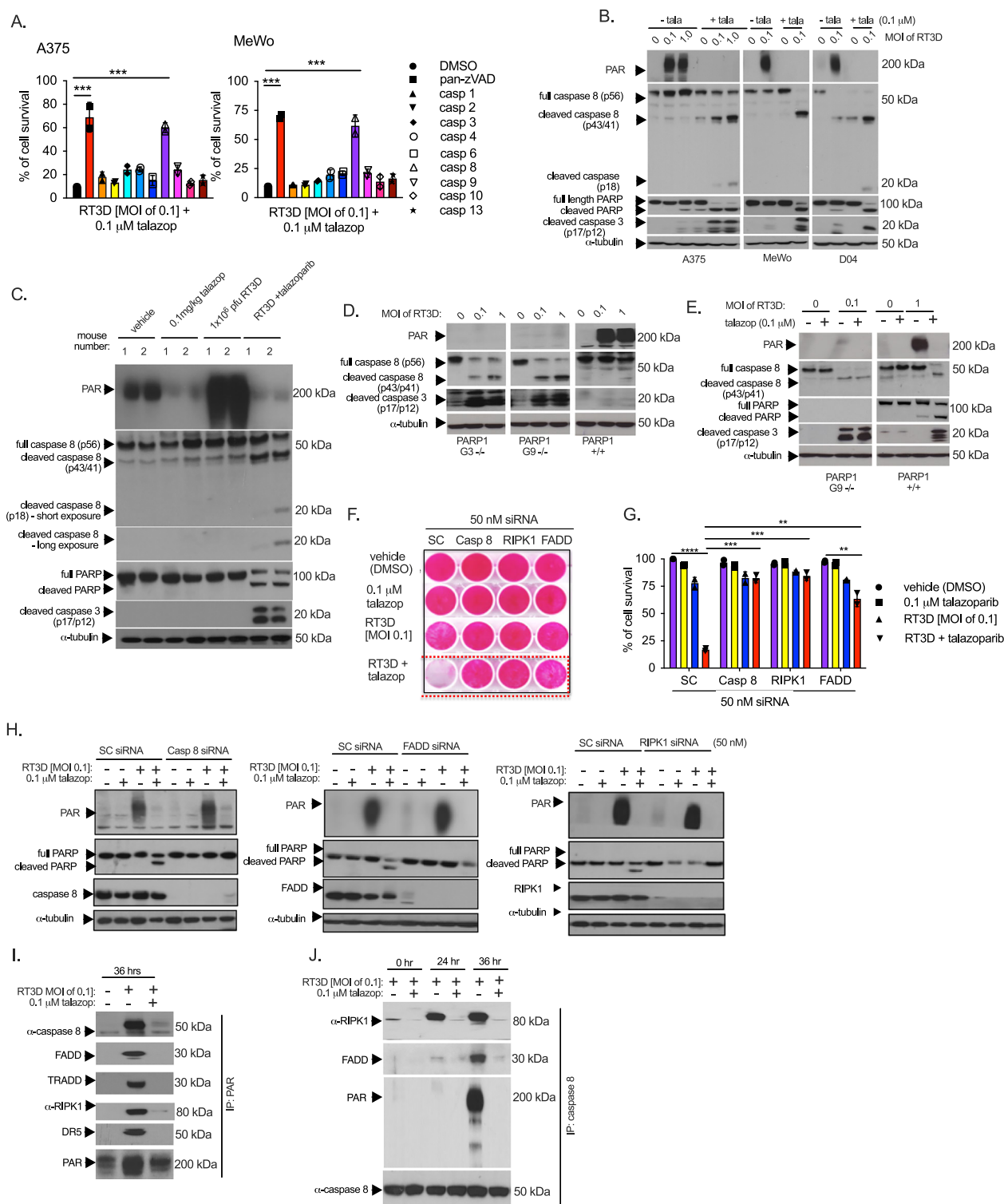


**Fig. 4 | RT3D plus talazoparib enhances death inducing signalling complex (DISC) mediated apoptosis.** **A** A375 or MeWo cells were treated with RT3D [MOI of 0.1] plus 0.1  $\mu$ M talazoparib in the presence of either pan-Caspase, or individual Caspase- inhibitors (all at 1 mM) and thereafter measured for cell survival using MTT. Data presented are mean values  $\pm$  SD,  $n = 2$  biologically independent experiments.  $P$  values were determined by one-way ANOVA corrected for multiple comparisons. **B** A375, MeWo and D04 cells were treated with 0.1  $\mu$ M talazoparib and thereafter infected with RT3D [MOI of 0.1] for 48 h. Western analysis was carried out to assess Caspase-8, Caspase-3 and PARP cleavage. Equal loading of proteins was assessed by probing for  $\alpha$ -tubulin. **C** CD1 nude mice bearing A375 tumour xenografts were treated with oral administration of vehicle (10% DMSO, 6% Solutol and 84% PBS) or 0.1 mg/kg talazoparib from Day 1–5. RT3D was injected intratumorally on Day 3 at  $1 \times 10^6$  pfu, or sham injection (PBS). Western analysis was carried out in A375 xenograft tumours for PAR, Caspase-8, Caspase-3 and PARP cleavage. Equal loading was measured by probing for  $\alpha$ -tubulin. **D** Western analysis was carried out in HeLa PARP-1 paired models. PARP-1<sup>+/+</sup> (wild type), and PARP-1<sup>-/-</sup> (clones G3 and G9) were infected with RT3D [MOI of 0.1 and 1.0] and immunoblotted for PAR, Caspase-8 and Caspase-3 cleavage. Equal loading was measured by probing for  $\alpha$ -tubulin. **E** Western analysis was carried out to assess PAR expression and cleavage of Caspase-3 and PARP, following treatment of talazoparib (0.1  $\mu$ M) in HeLa PARP-1<sup>+/+</sup> and PARP-1<sup>-/-</sup> (clone G9) cells. RT3D was then infected in the cells at MOI of 0.1 (PARP-1<sup>-/-</sup> clone G9) and MOI of 1.0 (PARP-1<sup>+/+</sup>). Equal loading was measured by probing for  $\alpha$ -tubulin. **F&G.** A375 cells were transfected with scramble

control (SC) or siRNA targeting RIPK-1, Caspase-8 or FADD (all at 50 nM) and subsequently treated with 0.1  $\mu$ M talazoparib and RT3D [MOI of 0.1] for 48 h and assessed by SRB cell viability assay. Data presented in **(G)** are mean values  $\pm$  SD,  $n = 2$  biologically independent experiments.  $P$  values were determined by two-way ANOVA corrected for multiple comparisons. **H** Western blot analysis was carried out in A375 cells transfected with scramble control (SC) or siRNA targeting Caspase-8, FADD, or RIPK1 all at 50 nM and subsequently treated with talazoparib and RT3D [MOI of 0.1] for 48 h. Lysates were immunoblotted for PAR, cleaved PARP-1, Caspase-8, FADD or RIPK1 to confirm siRNA target effect. **I** A375 cells were pre-treated with 0.1  $\mu$ M talazoparib and infected with RT3D at an MOI of 0.1 and immunoprecipitation (IP) assay with PAR antibody was carried out after 36 h. Western analysis was carried out to assess the interaction between PARylated proteins and the DISC components (Caspase-8, FADD, TRADD, RIPK1 and DR5). The input (lysate) was carried out to confirm RT3D induced PARylation (refer to supplementary Fig. 7A). **J** Caspase-8 immunoprecipitation was performed in A375 cells. Z-VAD (10 mM) was added in all samples prior to any treatment to prevent destabilisation of complexes with Caspase-8. Cells were then treated with RT3D [MOI of 0.1] and talazoparib (0.1  $\mu$ M) at 0, 24 and 36 h. Western analysis was carried out for PAR, RIPK1 and FADD antibodies. The input (lysate) was carried out to confirm expected RT3D induced PARylation and Caspase-8 cleavage. Equal loading was measured by probing for  $\alpha$ -tubulin (supplementary Fig. 7B).  $P$  values were derived where \* =  $p$  value, \*\* =  $p$  value < 0.01 and \*\*\* =  $p$  value < 0.001. Source data are provided as a source data file.

increase in PARP-1 and RIG-I interaction following RT3D infection and this was increased further by talazoparib treatment (Fig. 6E). Next, we assessed if similar PARP-1 and RIG-I interactions would occur following RT3D infection and co-treatment with other PARP-1 inhibitors (olaparib and veliparib) that are less potent than talazoparib. Interestingly, the interaction between PARP-1 and RIG-I appeared to be stronger and required a lower concentration of talazoparib (0.1–1  $\mu$ M) than was the case for olaparib, for which a concentration of 5–10  $\mu$ M was required. Veliparib showed hardly any interaction between PARP-1 and RIG-I, even at 10  $\mu$ M concentration (Fig. S11E).

It is interesting to note that the relative levels of PARP inhibitor-mediated modulation of the interaction between PARP-1 and a nucleic acid-bound PRR precisely mirrors the respective potencies of talazoparib (most), olaparib (intermediate) and veliparib (least) in terms of their abilities to trap PARP on sites of DNA damage, as confirmed in Fig. S11F. These data align with previous reports<sup>32,33</sup>. This observation raises the possibility that PARP inhibitors may have differential abilities to stabilise the PARP-1-RIG-I complex in a manner that may be analogous to PARP trapping on damaged DNA.

### Combination therapy of RT3D and talazoparib enhances anti-tumour efficacy in an immunocompetent animal model

We were keen to investigate whether the enhanced effects of RT3D/talazoparib on apoptosis and cytokine production resulted in increased immunogenicity in an immunocompetent in vivo tumour model. We firstly determined the effects on 4434 BRAF-mutant mouse melanoma cell lines in vitro to assess whether the RT3D plus talazoparib combination was acting in a similar fashion to the human cell lines. Indeed, addition of talazoparib enhanced the effects of RT3D as shown by MTT cell viability assay (Fig. S12A). Western blotting confirmed an increase in caspase-8, caspase-3 and PARP cleavage in response to RT3D/talazoparib compared to either agent alone (Fig. S12B). Furthermore, RT3D plus talazoparib-induced IFN- $\beta$  secretion (Fig. S12D) from supernatants collected from cells that were used to analyse SRB cell viability staining (Fig. S12C) and increase in IFN- $\beta$  correlated with an increase in dying cells.

Once we had confirmed that 4434 mouse BRAF-mutant melanoma cells had a similar phenotype to that of the human cell lines, we implanted them in an immunocompetent BL/6 mouse model and, once established, tumours were treated with RT3D, talazoparib or the combination (Fig. 7A). RT3D plus talazoparib led to a delay in tumour growth (Fig. 7B), and prolonged survival (Fig. 7C) versus single-agent

counterparts. Individual tumour volumes for each mouse ( $n$  of 6) per treatment group are summarised. All mice in the combination (RT3D/talazoparib) group were cured (6/6), compared to 2/6 in the single-agent counterparts (0.1 mg/kg talazoparib) or ( $1 \times 10^6$  pfu RT3D) as shown in the individual curves (Fig. S13A). Next, we assessed memory response in the cohort of mice that had been cured of 4434 tumours by re-challenging with 4434 cells on the contralateral flank. No tumour growth occurred in this cohort of mice (whilst, in parallel, naïve mice developed large tumours over time) (Fig. 7D).

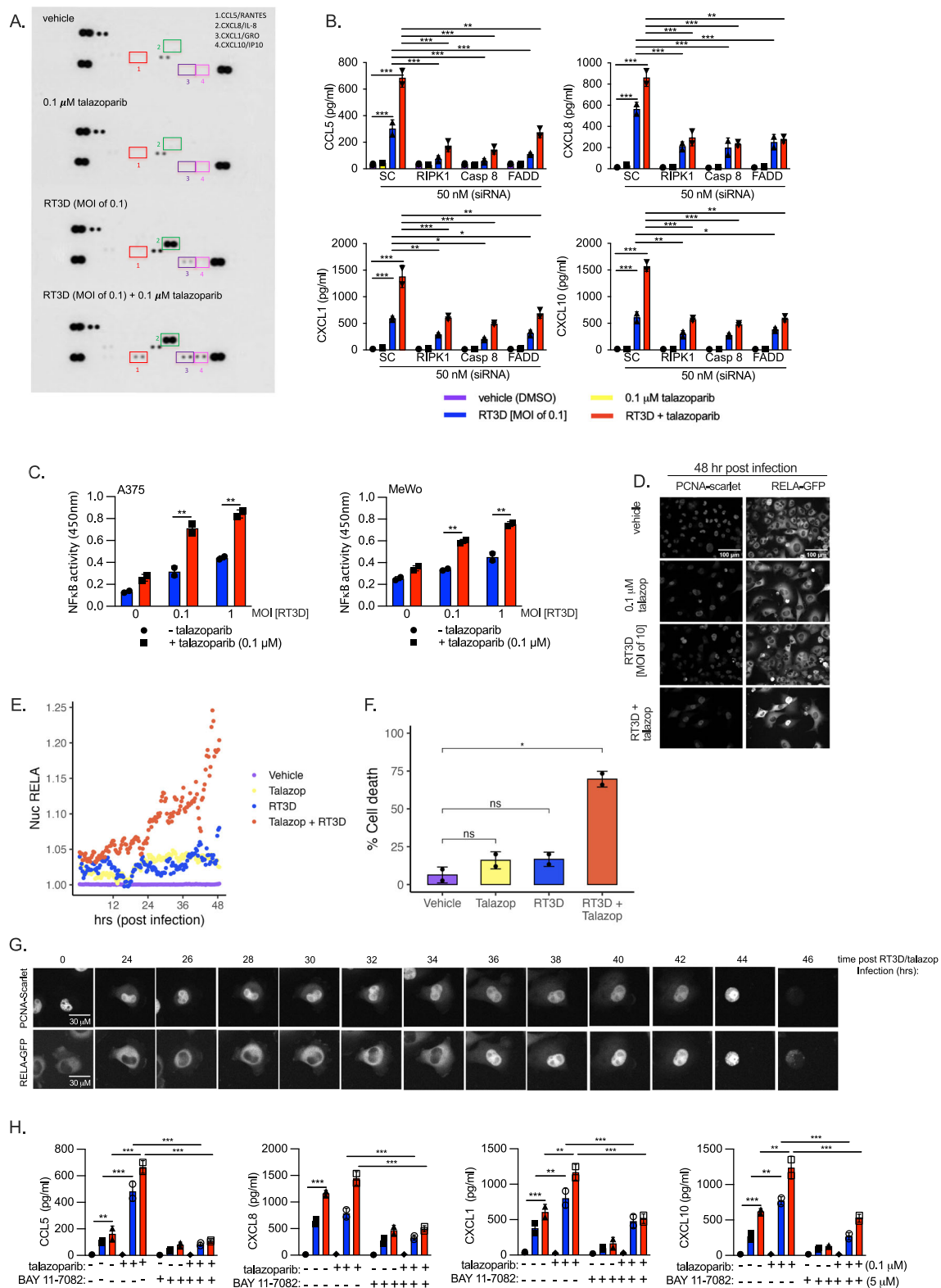
To probe further the impact of RT3D plus talazoparib therapy in vivo, total RNA was isolated and gene expression analysis was carried out in the tumour cells using the Nanostring nCounter technology platform, where deconvolution was carried out to characterise the immune pathways that were modulated following RT3D and talazoparib treatment. There were increases in tumour-infiltrating immune cells in the microenvironment by means of increased expression of transcripts associated with immune subsets (Fig. 7E).

In support of these findings, FACS analysis of in vivo tumour samples was carried out.

Tumour volumes of mice used to profile the immune infiltrate by FACS analysis were measured up to Day 12 (Fig. 7F) and their weights measured prior to profiling the immune infiltrate by FACS analysis at time of harvest (Fig. 7G). Our data revealed an increase of CD3<sup>+</sup>, CD8<sup>+</sup> and CD4<sup>+</sup> cells with RT3D plus talazoparib (Fig. 7H). There was no increase in foxp3<sup>+</sup> cells following RT3D injection, when compared to vehicle or talazoparib alone. These levels were increased following RT3D/talazoparib treatment, but this was non-significant (Fig. 7I). Additionally, PD-L1<sup>+</sup> and PD-1<sup>+</sup> cells were increased with treatment, providing rationale for future testing of RT3D and anti-PD-1 antibodies in combination with PARP inhibition (Fig. 7J). Gating strategies for Fig. 7G–J are provided in supplementary Fig. S13B.

## Discussion

By conducting a small-molecule drug screen, we have uncovered an unexpected role for PARP-1 in modulating RIG-I-mediated sensing and downstream signalling events in response to the presence of cytoplasmic dsRNA. We hypothesize that binding of viral dsRNA to RIG-I recruits PARP-1, which in turn, PARylates components of the extrinsic apoptotic signalling pathway and inhibits cellular apoptosis. Initially, we postulated that this is most likely a specific property of RT3D that would allow it to maintain cell viability long enough for successful completion of its replication cycle. Instead, however, the observation



that other non-viral dsRNA agonists can mediate signalling through RIG-I and recapitulate PARP-1 recruitment and inhibition of apoptosis points towards this being an important host defence mechanism to delay cell death and maintain, or even enhance, inflammatory signalling in response to a perceived viral infection. Interestingly, as anticipated, we found that pharmacological or genetic inhibition of the activity of PARP-1 led to enhanced extrinsic apoptosis pathway-driven

cytotoxicity but, rather counterintuitively, an even greater degree of NF- $\kappa$ B-mediated proinflammatory signalling. In an immunocompetent animal model, we demonstrated that the combination of RT3D and talazoparib achieved tumour control in all animals and this was associated with profound modulation of the tumour immune microenvironment and protection against subsequent isogenic tumour rechallenge. Taken together, these findings support clinical evaluation

**Fig. 5 | NF- $\kappa$ B activity and pro-inflammatory cytokine production is enhanced following RT3D and talazoparib treatment.** **A** A human cytokine array was used to assess cytokine secretion in A375 following RT3D [MOI of 0.1] and 0.1  $\mu$ M talazoparib 48 h post-treatment. **B** A375 cells were transfected with scrambled control (SC), RIPK1, Caspase-8 and FADD siRNA at 50 nM prior to treatment with 0.1  $\mu$ M talazoparib and RT3D [MOI of 0.1]. Supernatants were collected and assessed for CCL5/RANTES, CXCL8/IL8, CXCL1/GRO and CXCL10/IP10 cytokines by ELISA at 48 h post-infection. Data presented are mean values  $\pm$  SD,  $n = 2$  biologically independent experiments.  $P$  values were determined by two-way ANOVA corrected for multiple comparisons. **C** A375 and MeWo cell nuclear extracts were used to assess DNA binding activity of the NF- $\kappa$ B transcription factor RELA (p65) in nuclear extracts following exposure to RT3D [MOI of 0.1] and 0.1  $\mu$ M talazoparib at 48 h post-treatment. Data presented are mean values  $\pm$  SD,  $n = 2$  biologically independent experiments.  $P$  values were determined by two-way ANOVA corrected for multiple comparisons. **D** Representative images of PCNA-Scarlet (nuclear marker) and Rel-A GFP tagged A375 cells with RT3D [MOI of 10] and 1  $\mu$ M talazoparib treatment. **E** Rel-A GFP tagged A375 cells were treated with RT3D [MOI of 10] and

1  $\mu$ M talazoparib over a 48-h time-period. Cells were imaged by confocal microscopy and single cells tracked using automated imaging analysis Nuclear RELA was calculated as the total intensity in the nucleus region divided by the nucleus area. Data show the mean tracks of RELA over time. **F** Average percentage of single cell tracks corresponding to dying cells at 48 h post treatment. **G** Representative images of an A375 cell showing high nuclear RELA localisation eventually undergoing cell death following treatment with RT3D [MOI of 10] and 1  $\mu$ M talazoparib over a 48-h time-period. RELA-GFP translocates to the nucleus between 34 and 36 h post treatment and cell death is apparent from 44 h post treatment. **H** A375 cells were pre-incubated with the I $\kappa$ B phosphorylation inhibitor, BAY 11-7082 (5  $\mu$ M) and then treated with RT3D [MOI of 0.1] plus talazoparib (0.1  $\mu$ M). Supernatants were collected and assessed for CCL5/RANTES, CXCL8/IL8, CXCL1/GRO and CXCL10/IP10 cytokines by ELISA at 48 h post-infection. Data presented are mean values  $\pm$  SD,  $n = 2$  biologically independent experiments.  $P$  values were determined by two-way ANOVA corrected for multiple comparisons.  $P$  values were derived where \* =  $p$  value, \*\* =  $p$  value < 0.01 and \*\*\* =  $p$  value < 0.001. Source data are provided as a source data file.

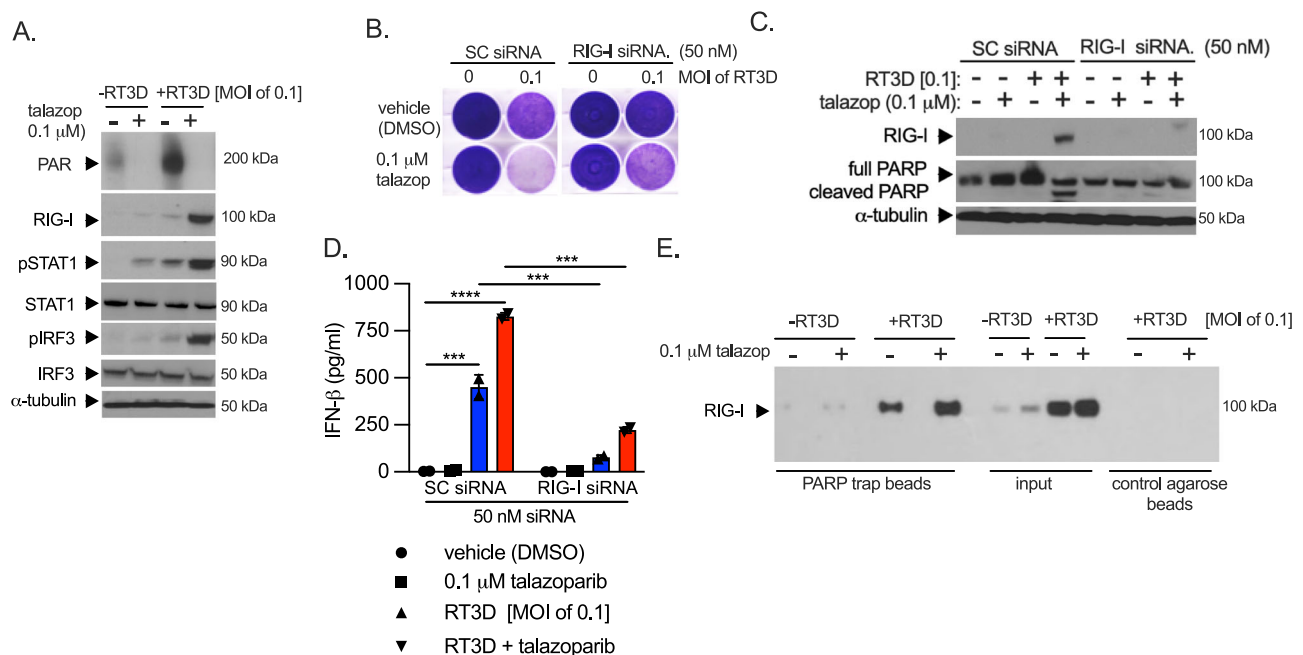


**Fig. 6 | Talazoparib enhances RT3D-induced interferon signalling through RIG-I.** **A** A375 cells were treated with talazoparib at 0.1  $\mu$ M and infected with RT3D [MOI of 0.1]. Western analysis was carried out to assess RIG-I, pSTAT-1, pIRF3, STAT1 and IRF3. Equal loading of proteins was assessed by probing for  $\alpha$ -tubulin. **B** A375 cells were transfected with non-targeting scrambled control (SC) siRNA or siRNA targeting RIG-I (50 nM) and thereafter treated with 0.1  $\mu$ M and RT3D [MOI of 0.1] for 48 h and assessed for cell viability as shown by crystal violet staining. **C** Western analysis was carried out on lysates from A375 cells and probed for RIG-I and cleaved

PARP, while **(D)** IFN- $\beta$  production was assessed by ELISA. Data presented are mean values  $\pm$  SD,  $n = 2$  biologically independent experiments.  $P$  values were determined by two-way ANOVA corrected for multiple comparisons. **E** A375 cells were treated with talazoparib at 0.1  $\mu$ M and RT3D [MOI of 0.1]. PARP-trap agarose IP was performed on the lysates and Western analysis carried out to assess interaction between PARP-1 and RIG-I.  $P$  values were derived where \* =  $p$  value, \*\* =  $p$  value < 0.01 and \*\*\* =  $p$  value < 0.001. Source data are provided as a source data file.

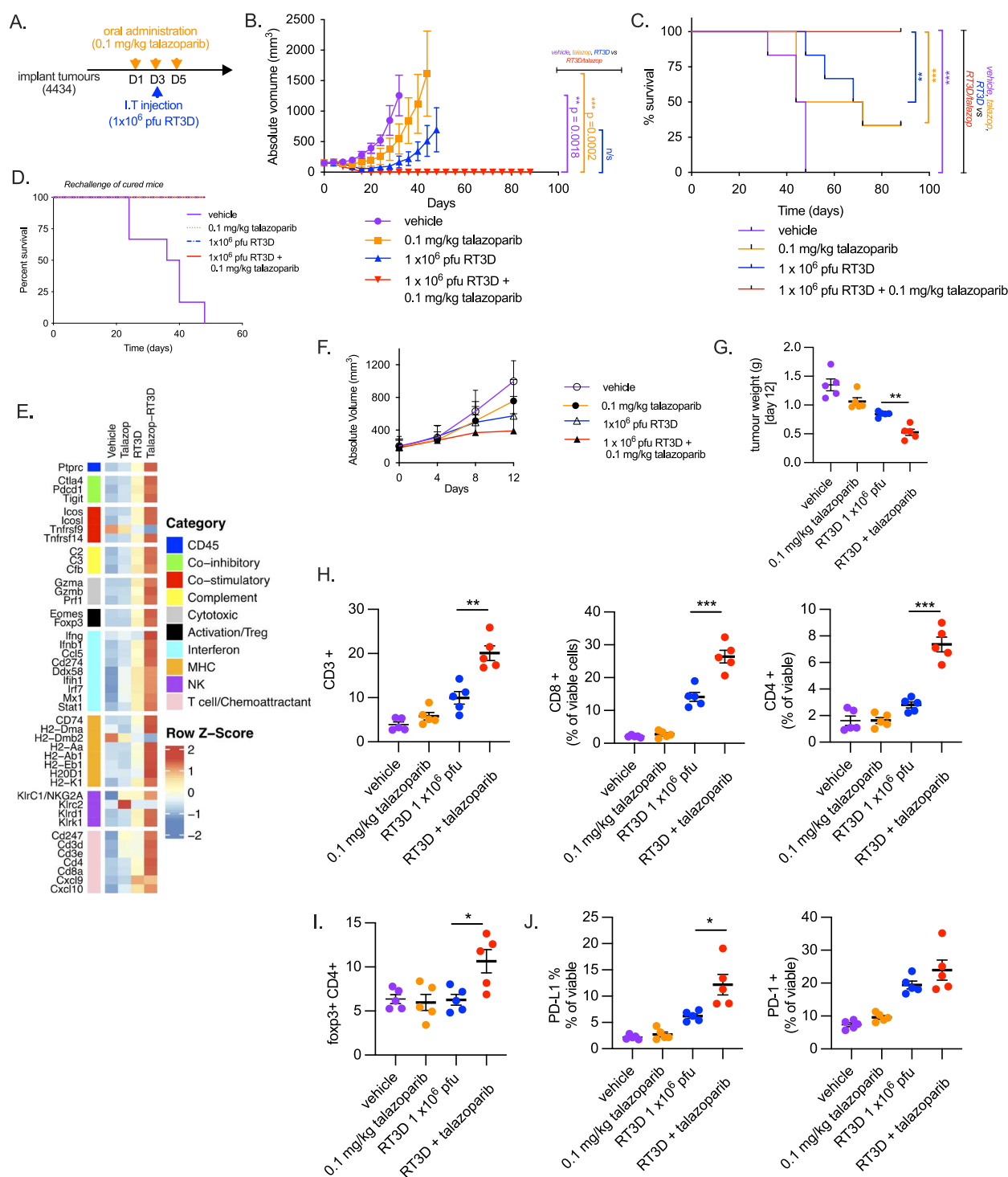
of combinations of agonists of dsRNA sensing with PARP inhibitors and offer the prospect of developing novel treatment approaches that extend the potential utility of PARP inhibition outside the current relatively narrow confines of HR-deficient cancers.

The initial screen in A375 melanoma cells highlighted talazoparib as a strong hit, with synergistic activity at sub micromolar drug concentrations across a range of viral MOIs. This finding was confirmed in multiple melanoma cell lines representing the main genetic contexts of that disease. Contrary to our initial hypotheses, combinatorial synergistic activity was due neither to cooperative enhancement of DNA damage nor increased viral replication-related oncolysis, effectively ruling out the primary purported mechanism of action of each of the respective partners of the combination. Intriguingly, RT3D infection was shown to activate cytoplasmic PARP-1

with resulting significant PARylation of cellular proteins. As expected, PARP inhibitors significantly reduced virally-induced PARylation, and this was associated with enhanced tumour cell kill. The effect was recapitulated in PARP-1<sup>-/-</sup> cells which showed exquisite sensitivity to RT3D but no combinatorial effect with PARP inhibition. Together, these data point to a role for PARP-1 in protecting cells from RT3D-induced cell death.

RT3D-induced cancer cell death involves TRAIL-mediated apoptosis and is associated with activation of Caspase-8-mediated extrinsic apoptosis<sup>26,27</sup>. While we observed an increase in RT3D-induced TRAIL and TNF plus their receptors, DR4/DR5, or TNFR1/TNFR2, respectively, this was not increased further by combination with talazoparib. Nonetheless, it is important to recognise that modulation of TRAIL/TNF $\alpha$  signalling may represent a means of enhancing the therapeutic





efficacy of RT3D/PARP inhibitor combinations. Immunoprecipitation for PARylated proteins pulled down DISC components (caspase-8, RIPK1 and FADD), suggesting a functional role for PARP-1 in limiting extrinsic apoptotic pathway signalling following RT3D infection alone. As further confirmation, by capturing with an anti-caspase 8 antibody, we pulled down DISC components, RIPK1 and FADD, and PARylated proteins. The addition of talazoparib markedly reduced the degree to which DISC components were pulled down by an anti-PAR antibody and this was associated, functionally, with significantly greater activity of the extrinsic apoptotic pathway. These data are consistent with previous reports of a novel function of PARP-1 in modulating caspase-8

following treatment with TRAIL, thereby inhibiting caspase-8 and limiting its function<sup>34</sup>.

Previous studies found caspase-8 can serve in two distinct roles in response to TRAIL receptor engagement: as a protease that promotes apoptosis; and as a scaffold for assembling a caspase-8-FADD-RIPK1 complex, leading to NF- $\kappa$ B dependent inflammation<sup>30</sup>. Furthermore, proapoptotic signals (such as Fas, TNF $\alpha$ , and TRAIL) were found to instigate the production of cytokines and perhaps influence immune responsiveness toward dying cells<sup>35</sup>. Similarly, our studies have confirmed that NF- $\kappa$ B activation occurs in response to RT3D therapy alone and that this is mediated by the DISC complex, as silencing of caspase-

**Fig. 7 | RT3D plus talazoparib enhances anti-tumour efficacy which correlates with an increase in immune response.** **A** Treatment schedule, black/6 mice carrying 4434 tumours were treated with oral administration of 0.1 mg/kg talazoparib or vehicle from Day 1–5. RT3D was injected intratumorally on Day 3 at  $1 \times 10^6$  pfu or sham injection. **B** Size of tumours were measured for each treatment cohort consisting of vehicle (10% DMSO, 6% Solutol and 84% PBS), 0.1 mg/kg talazoparib,  $1 \times 10^6$  pfu RT3D or combination. Each bar represents mean SEM  $\pm$  for each treatment group. **C** Kaplan–Meier curve was evaluated for each treatment group to assess the median survival rate. For (**B** and **C**), vehicle  $n = 6$ , RT3D  $n = 6$ , talazoparib  $n = 6$  and combination  $n = 6$  animals per group. **D** Mice cured at day 90 following talazoparib alone (2/6), RT3D alone (2/6) or RT3D plus talazoparib (6/6) were rechallenged on the other flank and compared with naïve mice injected with 4434 tumours (both implanted at  $4 \times 10^6$  cells) and tumor growth assessed. Control  $n = 6$ , RT3D  $n = 2$ , talazoparib  $n = 2$  and combination  $n = 6$  animals per group.

**E** Deconvolution of immune cells in 4434 tumours following RT3D and talazoparib treatment. Tumours were dissected on day 8 (3 mice per group) after treatment, total RNA was isolated and gene expression analysis performed using the mouse Immunology Profiling panel from NanoString Technologies. **F** Tumour volumes of mice used to profile the immune infiltrate by FACS analysis were measured up to Day 12 ( $n$  of 5). **G** Tumour weights of mice used to profile the immune infiltrate by FACS analysis at time of harvest were measured. **H** FACS analysis of in vivo tumour samples. Data show cell counts of CD3+, CD8+ and CD4+ cells gated from viable cells. **I** Cell counts of foxp3+ cells gated from viable cells. **J** Cell counts of PD-L1+ and PD-1+ cells gated from viable cells. For data sets (**F–J**), data presented are mean values  $\pm$  SEM from 1 biologically independent experiment. vehicle  $n = 5$ , RT3D  $n = 5$ , talazoparib  $n = 5$  and combination  $n = 5$  animals per group.  $P$  values were derived where \* =  $p$  value, \*\* =  $p$  value < 0.01 and \*\*\* =  $p$  value < 0.001. Source data are provided as a source data file.

8, FADD or RIPK1 attenuated NF- $\kappa$ B and its downstream pro-inflammatory cytokines (CCL5, CXCL1, CXCL8 and CXCL10). Critically, however, we have shown that co-treatment with RT3D and PARP inhibitor markedly enhances this NF- $\kappa$ B-mediated inflammatory signature, despite the fact that the combination prevents the block on extrinsic apoptosis mediated by PARylation of DISC components.

The dsRNA sensor, RIG-I, has previously been shown to promote apoptosis and cell death in hepatocellular carcinoma (HCC) whilst activating NF- $\kappa$ B in macrophages<sup>36</sup>. Combination of RT3D plus talazoparib significantly increased RIG-I expression and massively up-regulated RIG-I pathway components at the protein level, findings that correlated with the loss of PARylation. Our data point to a novel interaction between RIG-I and PARP-1, which is amplified following RT3D plus talazoparib treatment compared to either agent alone. We posit that, following binding to dsRNA (or its mimics), the dsRNA sensor, RIG-I, can bind to and activate PARP-1 and, thus, simultaneously inhibit extrinsic apoptosis and serve as a platform for inflammatory NF- $\kappa$ B signalling. We further propose that combination therapy with PARP inhibition effectively removes this PARylation-driven block on apoptosis but also functionally “traps” PARP-1 on dsRNA-bound RIG-I, in an analogous fashion to that described for PARP-trapping on DNA<sup>32,33,37,38</sup>. This leads to a phenotype of increased cancer cell death with enhanced cytokine production. Indeed, talazoparib has been shown to be a potent PARP-trapper on DNA, superior to either olaparib or veliparib (as confirmed in our own analyses). We confirmed talazoparib as a more effective and potent PARP-trapper on damaged DNA than either olaparib or veliparib, which correlated with greater efficacy of talazoparib in terms of triggering apoptosis, NF- $\kappa$ B signalling, cytokine production and RIG-I/PARP1 interaction.

In view of the relative complexity of using replication-competent, oncolytic viral agents in the clinic, we tested if other dsRNA agonistic therapies were able to phenocopy the cytotoxic and pro-inflammatory effects of RT3D. Importantly, we confirmed that both polyI:C and 3p-hRNA were able to mediate equivalent effects and this may accelerate opportunities for early-phase clinical evaluation of this approach. PolyI:C has previously been tested in the clinic both as a poly-lysine/carboxymethylcellulose-derivatized agent<sup>39</sup> and in nanoplexed format<sup>40</sup>. In addition, RIG-I agonism has also been tested in a phase I clinical trial as a single agent in combination with the anti-PD1 agent, pembrolizumab<sup>41</sup>.

At this point, given the pro-inflammatory nature of the RT3D and PARPi combination, we conducted preliminary profiling in an immunocompetent BRAF<sup>V600E</sup>-mutant murine melanoma model. Indeed, the combination therapy was highly effective, to an even greater degree to that seen in the immunodeficient human model. All combination therapy-treated animals were cured and protected from subsequent tumour rechallenge. Importantly, RNA sequencing and flow cytometric functional analyses confirmed dramatic pro-inflammatory changes within the tumour microenvironment of animals treated with the RT3D-PARPi combination. Furthermore, these data point

towards potentially effective additional combinations of dsRNA agonism, PARPi and immune checkpoint inhibition. Such approaches are the subject of ongoing work.

## Methods

### Cell lines

The following melanoma cell lines of known genetic background were used and obtained from stocks within Prof. Kevin Harrington's team, ICR London: A375 and Mel624 (V600E BRAF mutant), WM266.4 (V600D BRAF mutant), MeWo and PWMK (wild type RAS and BRAF). DO4 (N-RAS mutant) and WM17971 (K-RAS mutant) were obtained by generous donation from Prof. Richard Marais (The Paterson Institute of Cancer Research). The BRAF-mutant (BRAF<sup>V600E</sup>) mouse melanoma 4434 cell line was established from C57BL/6 BRAF+/LSL- BRAF<sup>V600E</sup>; Tyr::CreERT2+/c<sup>42</sup> and another kind donation from Prof. Richard Marais (The Paterson Institute of Cancer Research). HeLa PARP paired cell lines (wild type PARP<sup>+</sup>, PARP<sup>-</sup> [clone G3 and G9]) as well as HeLa clone A7 and F7 cells were obtained by generous donation from Prof. Christopher Lord, ICR London. All the cell lines were authenticated by using short tandem repeat (STR) profiling according to the manufacturer's instructions and were carried out by our in-house sequencing facility unit. Cells were cultured in DMEM or RPMI. Media was supplemented with 5% (v/v) FBS, 1% (v/v) glutamine and 0.5% (v/v) penicillin/streptomycin.

### Reovirus stocks

Reovirus Dearing type 3 (RT3D) stocks at  $3 \times 10^9$  tissue culture infectious dose 50 (TCID<sub>50</sub>/ml) were obtained from Oncolytics Biotech and stored at 1:10 concentrations in PBS at  $-80^\circ\text{C}$ .

### Drug screen and Cell Titer Glo (CTG) assay

A375 cells were plated at 500 cells per well in 20  $\mu\text{L}$ , in 384 well plates using a Thermo Scientific multidrop combi and incubated overnight. The following day, an in-house drug screen (Plate 11 and 12) comprising of 80 different chemotherapeutic and targeted therapy drugs (Supplementary Table S1) was used to treat the A375 melanoma cells with doses of drugs ranging from 0.0005  $\mu\text{M}$  to 1.0  $\mu\text{M}$ . RT3D was infected into the cells [MOI ranging between 0.01 and 5.0] 2-h post treatment of the drugs. Cell viability was measured by CellTiter-Glo Luminescent Cell Viability Assay (G9681, CTG, Promega, UK) at 72 h post treatment. We estimated the effect of each small molecule inhibitor on RT3D by calculating drug effect (DE) robust Z scores, with values  $< -2$  being considered a profound sensitisation effect<sup>43,44</sup>.

### Caspase inhibitor experiments

The caspase inhibitor sample pack (R&D systems-Cat No FMKAP01); which contained Z-VAD (general caspase inhibitor); Z-WEHD (caspase-1 inhibitor); Z-VDVAD (caspase-2 inhibitor); Z-DEVD (caspase-3 inhibitor); Z-YVAD (caspase-4 inhibitor); Z-VEID (caspase-6 inhibitor); Z-IETD (caspase-8 inhibitor); Z-LEHD (caspase-9 inhibitor); Z-AEVD

(caspase-10 inhibitor) and Z-LEED (caspase-13 inhibitor) were used at 10  $\mu$ M each to inhibit the relevant caspase inhibitors in A375 and MeWo cells 8 h prior to RT3D (MOI of 0.1) plus 0.1  $\mu$ M talazoparib treatment.

### Small interfering RNA transfections

3 or  $5 \times 10^5$  cells were seeded out in the appropriate media without penicillin-streptomycin. Twenty-four hours after seeding, siRNA transfections were done on sub confluent cells incubated in unsupplemented OptiMEM using the Lipofectamine RNAiMAX transfection reagent (13778100, Thermo Fisher) according to the manufacturer's instructions. After 24 h, media was changed, and the appropriate treatment carried out for 48 h. Lysates were collected for Western analysis, ELISA or cell death by SRB assay. All the siRNAs were purchased from Qiagen. We used two pooled siRNAs for PARP-1, 2 and 3 siRNAs: Hs PARP1\_5 FlexiTube siRNA (SI02662989), Hs PARP1\_6 FlexiTube siRNA (SI02662996); Hs PARP2\_2 FlexiTube siRNA (SI00077917), Hs PARP2\_3 FlexiTube siRNA (SI00077924); Hs PARP3\_1 FlexiTube siRNA (SI00077938), Hs PARP3\_4 FlexiTube siRNA (SI00077959). For the death inducing signaling complex (DISC), we used Caspase 8\_11 FlexiTube siRNA (SI02661946); Hs RIPK1\_5 FlexiTube siRNA (SI00288092); Hs FADD siRNA (hsFADD 7; hsFADD 5; hsFADD 8; hsFADD 9) and for the RIGI/IFN- $\beta$  pathway, we used RIGI FlexiTube siRNA (GS23586).

### 3-(4,5-dimethylthiazol-2-yl)-2,5-diphenyltetrazolium bromide (MTT) assay

Cell viability was quantified using a 3-(4,5-dimethylthiazol-2-yl)-2,5-diphenyltetrazolium bromide (M6494, Sigma-Aldrich), MTT assay. Briefly 20  $\mu$ l MTT at 5 mg/ml in PBS was added to treated cells in a 96-well plate. After 4 h incubation at 37 °C, crystals were solubilised in DMSO, and absorbance was measured at 570 nm on a SpectraMax 384 plate reader (Molecular Devices).

### Crystal violet and sulforhodamine B (SRB) assays

Cell viability was quantified by staining with crystal violet (HT90132, scientific laboratory supplies). For SRB assays, cells were fixed in 10% trichloroacetic acid (TCA) for 1 h, washed in tap water left to dry prior to staining with 0.057% SRB (wt/vol, 341738, Sigma-Aldrich). The crystal violet-stained images of the plate were captured on a Microtek ScanMaker 8700 (Microtek International Ltd) while the SRB-stained cells were diluted with 1 mM TRIS and absorbance was measured at 570 nm on a SpectraMax 384 plate reader.

### Reovirus replication assays

A375, MeWo and D04 cells were seeded in 24-well plates at a density of  $1 \times 10^5$  cells/well. The next day cells were treated with 0.1  $\mu$ M talazoparib and infected with RT3D at an MOI of 5 for 2 h. The cells were washed twice in complete growth media. Complete growth media was added to the cells and incubated at 37 °C. The cells were harvested, and the supernatants were collected at 4-, 24-, and 48-h post-infection in triplicate. The lysates had three freeze-thaw cycles between -80 °C and room temperature. For one-step growth curves the resulting lysates were titrated on L929 cells in 96-well plates. Viral titers were determined using the TCID<sub>50</sub>/method to calculate the infectious titer of virus in a sample, by diluting the sample across target cells and measuring cytopathic effect<sup>45</sup>. For plaque assays, dilutions were used to infect L929 cells seeded at  $2 \times 10^5$  cells/well in 6-well plates. After incubation at 37 °C for 4 h, the viral medium was removed and the wells overlaid with a 1:1 solution of 2% agar (Sigma) and 2 $\times$  DMEM containing 5% (v/v) FCS, 1% (v/v) glutamine, and 0.5% (v/v) penicillin/streptomycin. After 5 days, plates were stained with 0.2% crystal violet in 7% ethanol. Plates containing plaques were scanned and counted using Open CFU software<sup>46</sup>. Data from the viral growth curves were derived by TCID<sub>50</sub> or total viral titer quantified by plaque assays on confluent L929 cells.

### Cell cycle

Cells were seeded in 6-well dishes at  $3 \times 10^5$  cells/well and the next day treated with 0.1  $\mu$ M talazoparib and/or RT3D (MOI of 0.1) accordingly. Cells were fixed with 70% ethanol at indicated time points and stained with propidium iodide (PI, P4864, Sigma-Aldrich) at 1  $\mu$ g/mL. Flow cytometry analysis was performed using a LSRII flow cytometer (BD Biosciences, Oxford, UK).

### Cell death (Celigo) assay

Cells were seeded at  $8 \times 10^3$  in 96-well plates (#655090, Greiner) and 24 h later treated accordingly with talazoparib and/or RT3D for 48 h post-infection. Hoechst (0.5  $\mu$ g/ml) and PI (1  $\mu$ g/ml) were added, and the percentage of dead cells was measured using the Celigo S Cell Imaging Cytometer (Nexcelon Bioscience). The percentage of dead cells was calculated by measuring the total number of cells (nuclei staining-Hoechst) while simultaneously measuring PI (P4864, Sigma-Aldrich) positive (dead cells) in the whole well.

### Confocal imaging

Cells were plated in 35 mm glass-bottomed, collagen-coated dishes (MatTek, Massachusetts, USA) and the next day treated with talazoparib and RT3D accordingly. 24 h post-infection, cells were fixed with 4% formaldehyde and immunofluorescence performed. Cells were stained with  $\gamma$ -H2AX (S139) clone 20E3 (New England BioLabs, UK) or 53BP1 clone 6B3E10 (Santa-Cruz) and visualized using Alexafluor-488-conjugated goat anti-rabbit and Alexafluor-546-conjugated goat anti-mouse antibodies (Invitrogen™, Life Technologies) along with 4',6-diamidino-2-phenylindole, dihydrochloride (DAPI; Invitrogen, Molecular Probes™) nuclear stain. Cells were imaged using a LSM 710 inverse laser scanning microscope (Zeiss) and captured with a LSM T-PMT detector (Zeiss). Nuclei were quantified as positive for foci when  $\geq 5$  foci were present within the nucleus, for  $\gamma$ -H2AX or 53BP1.

### COMET assay

Cells were plated at  $3 \times 10^5$  in 6-well plates and the next day treated with 0.1  $\mu$ M talazoparib and/or RT3D (MOI of 0.1) for 48 h post infection. Cells were thereafter trypsinised and combined 1:8 with 1% low melting point agarose, placed onto a 1% normal melting point agarose pre-coated slide and cover slipped on ice for 5 min before lysis (NaCl 2.5 M, EDTA disodium salt 100 mM and Tris base 10 mM in distilled water, adjusted to pH10.5 with NaOH, 1% DMSO and 1% Triton  $\times$ -100) for 1 h at 4° in the dark. Slides were placed in an electrophoresis tank with 300 mM NaOH, 1 mM EDTA and 1% DMSO for 30 min before electrophoresis at 25 V, 300 mA, neutralised with 500 mM Tris-HCl, pH 8.0; DNA was stained using SYBR-safe (ThermoFisher) and imaged using a Zeiss LSM710 confocal microscope. A minimum of 115 cells were analysed from 2 independent replicates and percent tail DNA was calculated using OpenComet 1.3 plugin for ImageJ<sup>47</sup>.

### Western blotting

Cells were plated at  $0.5 \times 10^6$  in 60 mm dishes. The following day, cells were treated accordingly and collected between 24 and 72 h post-treatment. Cells were washed in ice-cold PBS, pelleted and resuspended in radioimmunoprecipitation assay buffer [50 mM Tris (pH 7.5), 150 mM NaCl, 1% NP40, 0.5% sodium deoxycholate, and 0.1% SDS] with protease inhibitors (Roche Diagnostics GmbH, Mannheim, Germany), 1 mM sodium orthovanadate (S6508, Sigma-Aldrich), and 10 mM sodium fluoride. Cells were then lysed by snap freezing on dry ice and then allowing the lysate to thaw on ice for 10 min. The lysate was centrifuged at  $8000 \times g/4$  °C for 20 min to remove cell debris. Protein concentration was determined using the BCA protein assay reagent (Pierce, Rockford, IL). 30  $\mu$ g of each protein sample were resolved on SDS-polyacrylamide gels (10–12%) and transferred to a polyvinylidene difluoride (PVDF) Hybond-P membrane (Amersham, Buckinghamshire, UK). Immunodetections were performed using antibodies provided in



supplementary Fig. 5. Equal loading was assessed using  $\alpha$ -tubulin. Blots were developed using secondary antibody (anti-rabbit or anti-mouse) conjugated to horseradish peroxidase (GE-Healthcare). The Super Signal chemiluminescent system (Pierce) or Immobilon Western chemiluminescent HRP substrate (Millipore) were used for detection. Uncropped scans of Western blots are provided in the source data file.

### Immunoprecipitation assays

Complex II purification for caspase 8 immunoprecipitation (IP) was essentially performed<sup>48–50</sup>. Briefly, cells were seeded in 10 cm dishes and treated as indicated in figure legends. After stimulation, media was removed and plates were washed with ice cold PBS to stop stimulation and frozen at  $-80^{\circ}\text{C}$ . Plates were thawed, and cells lysed in DISC lysis buffer (20 mM Tris pH 7.5, 150 mM NaCl, 2 mM EDTA, 1% Triton  $\times$ 100 and 10% glycerol) supplemented with protease inhibitors and PR619 (10  $\mu\text{M}$ ). Cells were lysed on ice and lysates were rotated at  $4^{\circ}\text{C}$  for 20 min and then clarified at  $4^{\circ}\text{C}$  at  $8000 \times g$  for 10 min. 20  $\mu\text{L}$  of protein G Sepharose (Sigma) with Casp-8 (C20) antibody (Santa Cruz Biotechnology) at 1.5  $\mu\text{g}$  antibody/mg protein lysate were rotated with cleared protein lysates overnight at  $4^{\circ}\text{C}$ . Similarly, for PAR immunoprecipitation, cells lysates were made in immunoprecipitation lysis buffer (1% Triton  $\times$ 100, 50 mM Tris pH 7.5, 150 mM NaCl, 5 mM EDTA + inhibitor cocktail tablets). 1  $\mu\text{g}$  of PAR antibody was added to lysates and subsequently incubated with 50  $\mu\text{L}$  of 1:1 slurry of protein G-agarose beads overnight at  $4^{\circ}\text{C}$ . The next day, 4 $\times$  washes in wash buffer (50 mM Tris pH 7.5, 150 mM NaCl, 0.1% Triton  $\times$ 100, and 5% glycerol) were performed, and samples eluted by boiling in 50  $\mu\text{L}$  1 $\times$  SDS loading dye. Protein samples for both caspase 8 IP and the PAR IP were resolved on SDS-polyacrylamide gels (10–12%) and transferred to a polyvinylidene difluoride (PVDF) Hybond-P membrane (Amersham, Buckinghamshire, UK) as described above in the Western blot analysis section.

### Immunoprecipitation of PARP-1 using the PARP1-Trap Agarose kit

We used the PARP1-Trap Agarose kit [xtak-20] from Chromotek, which consists of a PARP1 Nanobody/ VHH, coupled to agarose beads to immunoprecipitate endogenous PARP-1 proteins. Briefly, cells were harvested with Lysis Buffer: 50 mM Tris-HCl pH 7.5, 150 mM NaCl, 5% glycerol, 0.5% NP-40, 5 mM  $\text{MgCl}_2$ , 0.2 mM  $\text{CaCl}_2$ , 1  $\mu\text{M}$  pepstatin A, 1  $\mu\text{M}$  bestatin supplemented with protease inhibitor cocktail. DNase I (75–150 Kunitz U/mL) was then added to lysates and incubated for 1 h at  $4^{\circ}\text{C}$  with rotation. Lysates were centrifuged at  $4^{\circ}\text{C}$  for 10 min at  $17,000 \times g$ , and cleared supernatants transferred to a pre-cooled tube. PARP1-Trap beads were incubated with lysates for 3 h at  $4^{\circ}\text{C}$  with rotation. Next, agarose beads were washed three times with 0.5 ml of wash buffer (50 mM Tris-HCl pH 7.5, 150 mM NaCl, 5% glycerol and 0.5% NP-40). Bound proteins were eluted with NuPAGE LDS sample loading buffer and heated at  $95^{\circ}\text{C}$  for 5 min with 10 mM DTT.

### Fractionation of PARP-DNA complexes

A375 cells were treated with talazoparib, olaparib or veliparib in the presence or absence of RT3D for 48 h, harvested with trypsin-EDTA and thereafter centrifuged at  $500 \times g$  for 5 min. A subcellular protein fractionation kit (Thermo Scientific 78840) using different stringency buffers was used according to the manufacturer's instructions. Briefly, A375 cells were fractionated using different stringency buffers with stepwise separation and preparation of cytoplasmic, membrane, nuclear soluble and chromatin-bound protein extracts. The first reagent (cytoplasmic extraction buffer [100 mM MES-NaOH, pH 6.4, 1 mM EDTA and 0.5 mM  $\text{MgCl}_2$ ] with protease inhibitors plus Complete Mini, 1 836 153, Roche, Mannheim, Germany) was added to the cell pellets leading to selective cell membrane permeabilization and releasing soluble cytoplasmic contents. The second reagent

(membrane extraction buffer [50 mM HEPES-NaOH, pH 7.5, 250 mM KCl, 2.5 mM  $\text{MgCl}_2$ , 0.05% Triton  $\times$ 100] and protease inhibitors) dissolved plasma, mitochondria and ER/golgi membranes but did not solubilize nuclear membranes. After recovering the intact nuclei by centrifugation, a third reagent: nuclear extraction buffer [50 mM HEPES-NaOH, pH 7.5, 500 mM KCl, 2.5 mM  $\text{MgCl}_2$ , 0.1% Triton  $\times$ 100] and protease inhibitors) yielded the soluble nuclear extract. A second nuclear extraction with 5 mM  $\text{CaCl}_2$  plus 3 units micrococcal nuclease (MnNase) was performed to release chromatin-bound nuclear proteins. The supernatants for nuclear and chromatin fractionation were run for Western blot analysis and probed for PAR [4335-MC-100] from Trevigen, PARP-1 (clone F2) [sc-8007] from Santa Cruz, and Histone H3 [07-690] from Upstate Biotechnology.

### Proteome profiler human cytokine array

Cells were plated at  $3 \times 10^5$  cells per well in 6-well plates and media collected 48 h after treatment with RT3D-talazoparib then centrifuged to remove cells or debris. The activity of 36 human cytokines, chemokines and acute phase proteins were simultaneously assessed using the proteome profiler human XL cytokine array kit [ARY005B] from R&D Systems (Abingdon, UK). Cell lysates were obtained from A375 following treatment with 0.1 MOI of RT3D and 0.1  $\mu\text{M}$  talazoparib at 48 h post-treatment. Cytokine secretion was carried out as a validation from the results of the human cytokine array using a range of human ELISAs from R&D Systems (see below).

### Enzyme-linked immunosorbent assay (ELISA)

Cells were plated at  $2 \times 10^5$  cells per well in 24-well plates and treated accordingly. The cells were collected at the appropriate time point and measured a range of human DuoSet ELISAs according to the manufacturer's protocol. The following cytokines/chemokines were assessed for secretion in the cells following treatment: CCL5/RANTES [DY278], CXCL1/GRO $\alpha$  [DY275], CXCL10/IP-10 [DY266] and CXCL8/IL-8 [DY208] and TRAIL/TNFSF10 [DY375], all from R&D systems. The TNF high sensitivity ELISA [BE58351] was sourced from Tecan (IBL).

### NF- $\kappa\text{B}$ p65 transcription factor assay

We extracted nuclear and cytoplasmic fractionation of A375 and MeWo cells following treatment according to manufacturer's instructions (Abcam, ab113474). Briefly, cells were collected and pelleted by centrifugation then pellets were thereafter re-suspended using pre-extraction buffer from the kit. The supernatant containing cytoplasmic fraction was frozen down and stored. The pellet was centrifuged once again and re-suspended in nuclear extraction buffer from the kit to generate the nuclear fraction and samples used for the NF- $\kappa\text{B}$  p65 transcription ELISA based assay (Abcam, ab133112) according to the manufacturer's instructions.

### Live cell imaging and analysis

RELA and PCNA were fluorescently tagged at the endogenous loci using CRISPR-CAS9 gene editing to generate RELA-eGFP and PCNA<sup>31</sup>. Briefly, A375 cells were imaged at 20 min intervals following RT3D 10 MOI addition with 2 h 1  $\mu\text{M}$  talazoparib pre-treatment. Cells were imaged using the Zeiss Axio Observer Z1 Marianas Microscope with a CSUX1 confocal spinning disk unit built by 3i (Intelligent Imaging Innovations; Denver, CO). During imaging, cells were maintained at  $37^{\circ}\text{C}$  with  $>60\%$  humidity and 5%  $\text{CO}_2$ . Live imaging analysis was carried out using Nuclitrack software. Nuclear RELA was calculated as the total intensity in the nucleus region divided by the nucleus area using Harmony software (PerkinElmer).

### Proteomics and LC-MS/MS analysis

Cells were seeded in 6 cm dishes at  $9 \times 10^5$  cells per well overnight prior to treatments and collected at indicated time-points by trypsinising



cells and washing 3 times in PBS. Pellets were stored at  $-80^{\circ}\text{C}$  prior to processing. The cell pellets were lysed in 5% SDS/100 mM TEAB (tetraethylammonium bromide, Sigma) by ultrasonic probe process at 40% power for 15 s on/1 s off, heated at  $90^{\circ}\text{C}$  for 10 min, and then processed by ultrasonic probe again as above. The lysate was centrifuged at  $8000 \times g$  for 15 min. The supernatant was collected, and protein concentration was measured by Pierce 660 nm Protein Assay (ThermoFisher Scientific) and 80  $\mu\text{g}$  of proteins per sample used. Proteins were reduced by TCEP (Tris(2-carboxyethyl) phosphine, Sigma), alkylated by iodoacetamide (Sigma), and then precipitated by 20% TCA (trichloroacetic acid, Sigma) to remove detergent and excessive reagent. Protein pellet was resuspended in 80  $\mu\text{l}$  of 100 mM TEAB buffer, and 3.2  $\mu\text{g}$  trypsin (Pierce MS grade, ThermoFisher Scientific) was added, and the digestion went on 18 h at  $37^{\circ}\text{C}$ . Then 40  $\mu\text{g}$  of protein digest was taken and labelled by 0.4 mg TMT11plex. 11 samples were pooled and dried in SpeedVac (Thermo Scientific). The dried peptide mixture was resuspended in 0.1%  $\text{NH}_4\text{OH}/100\% \text{H}_2\text{O}$ , and fractionated on an XBridge BEH C18 column (2.1 mm i.d.  $\times$  150 mm, Waters) with an initial 5 min loading then linear gradient from 5% ACN/0.1%  $\text{NH}_4\text{OH}$  (pH 10)–35%  $\text{CH}_3\text{CN}/0.1\% \text{NH}_4\text{OH}$  in 30 min, then to 80%  $\text{CH}_3\text{CN}/0.1\% \text{NH}_4\text{OH}$  in 5 min and stayed for another 5 min. The flow rate was at 200  $\mu\text{l}/\text{min}$ . Fractions were collected at every 30 s from retention time at 3 min to 44 min, and then concatenated to 51 fractions and dried in SpeedVac. The peptides were reconstituted in 30  $\mu\text{l}$  of 0.1% FA/ $\text{H}_2\text{O}$  and 50% was injected for on-line LC-MS/MS analysis on the Orbitrap Fusion Lumos hybrid mass spectrometer coupled with an Ultimate 3000 RSLCnano UPLC system (ThermoFisher Scientific). Samples were first loaded and desalted on a PepMap C18 nano trap (100  $\mu\text{m}$  i.d.  $\times$  20 mm, 100  $\text{\AA}$ , 5  $\mu\text{m}$ ) then peptides were separated on a PepMap C18 column (75  $\mu\text{m}$  i.d.  $\times$  500 mm, 2  $\mu\text{m}$ ) over a linear gradient of 8–32%  $\text{CH}_3\text{CN}/0.1\% \text{FA}$  in 90 min, cycle time at 120 min at a flow rate at 300 nL/min. The MS acquisition used MS3 level quantification with Synchronous Precursor Selection (SPS) with the Top Speed 3 s cycle time. Briefly, the Orbitrap full MS survey scan was  $m/z$  375–1500 with the resolution 120,000 at  $m/z$  200, with AGC set at  $4 \times 10^5$  and 50 ms maximum injection time. Multiply charged ions ( $z = 2\text{--}5$ ) with intensity threshold at  $1 \times 10^4$  were fragmented in ion trap at 35% collision energy, with AGC at  $1 \times 10^4$  and 50 ms maximum injection time, and isolation width at 0.7 Da in quadrupole. The top 5 MS2 fragment ions were SPS selected with the isolation width at 0.7 Da, and fragmented in HCD at 65% NCE, and detected in the Orbitrap to get the report ions' intensities at a better accuracy.

### Whole proteome data analysis

Raw spectra were processed using Proteome Discoverer v2.4 (ThermoFisher Scientific) and searched against FASTA sequence databases containing GENCODE v32<sup>51</sup> protein sequences, UniProt (2019\_05) Reovirus Proteins, translated gVE database<sup>52</sup> sequences and cRap contaminants using both Mascot server v2.4 (Matrix Science) and SequestHT with target-decoy scoring evaluated using Percolator<sup>53</sup>. The precursor tolerance was set at 20 ppm, fragment tolerance set at 0.5 Da and spectra were matched with fully tryptic peptides with a maximum of two missed cleavages. Fixed modifications included: carbamidomethyl [C] and TMT6plex [N-Term]. Variable modifications included: TMT6plex [K], oxidation [M], and deamidation [NQ]. Peptide results were initially filtered to a 1% FDR (0.01  $q$ -value). The reporter ion quantifier node included a TMT-11-plex quantification method with an integration window tolerance of 15 ppm and integration method based on the most confident centroid peak at MS3 level. Protein quantification was performed using unique peptides only, with protein groups considered for peptide uniqueness. Log2 fold change ratios were calculated for each sample vs time point basal sample using normalised protein abundances. Ratios and abundance were loaded into Perseus<sup>54</sup> or further downstream analysis and plotting. Z-score scaling was used to generate heatmaps, proteins were clustered using k-means method

and GO enrichment was performed using Fisher exact test. Results and RAW spectral files have been uploaded to PRIDE repository<sup>55</sup> under project accession [PXD047621](https://doi.org/10.1038/s41467-025-61297-w).

### Quantitative RT-PCR

RNA was extracted from samples using Qiagen RNeasy kit (74134, Qiagen, UK), and cDNA synthesized using SensiFAST cDNA synthesis kit (BIO-65053, Bioline). Samples were then amplified against transcripts by qRT-PCR with SYBR green (BIO-92005, Bioline). Primers used are provided in Supplementary Table 3. Relative gene expression was calculated by using beta actin as the housekeeping gene. All kits were used as per manufacturers' instructions and all qPCR assays were carried out using Step One Real-Time PCR System (Applied Biosystems).

### In vivo studies

All procedures were approved by the Animal Welfare and Ethical Review Board at the Institute of Cancer Research in accordance with Home Office Regulations under the Animals (Scientific Procedures) Act 1986. All animals were handled according to the Institute and U.K. Home Office guidelines and kept in a specific pathogen-free facility and exposed to a 12 h light/dark cycle at a constant temperature ( $22 \pm 2^{\circ}\text{C}$ ), with access to unrestricted food and water supply. All animals in this study are commercially available and were purchased from Charles River. Two in vivo models were used in this study. Stock numbers for purchased animals are 000664 for C57BL/6 mice and 086 for CD1 nude mice. A375 BRAF<sup>V600E</sup>-mutant melanoma tumours were established in 6–8 week old female CD1 nude mice, or 4434 BRAF<sup>V600E</sup>-mutant melanoma tumours established in 6–8 week old female C57BL/6 immunocompetent mice by subcutaneous injection of  $5 \times 10^6$  (A375) or  $4 \times 10^6$  (4434) cells suspended in 100  $\mu\text{l}$  PBS in the right flank. Once tumours were established and reached approximately 75–100  $\text{mm}^3$ , mice were allocated into treatment groups stratified by tumour size before beginning therapy. talazoparib (0.1 mg/kg) or vehicle (10% DMSO, 6% Solutol, and 84% PBS) was administered by oral gavage, on day 1, 3 and 5, while  $1 \times 10^6$  pfu RT3D dissolved in PBS was administered by intra-tumoral injection after talazoparib treatment on day 3. In the CD1 models, A375 tumours from 2 mice from each group were harvested on the last day of treatment and homogenized in PBS on ice and protein extracted with Lysis Buffer [25 mM Tris (pH 7.5), 150 mM NaCl, 5 mM EDTA, 2 mM EGTA, 1% Triton  $\times$ -100, sodium deoxycholate, and 0.1% SDS] with protease inhibitors (Roche Diagnostics GmbH, Mannheim, Germany), 1 mM sodium orthovanadate (S6508, Sigma-Aldrich), and 10 mM sodium fluoride. Caspase-8, caspase-3 and PARP cleavage were determined by Western Blot analysis, while levels of PAR in the tumour lysates were determined by ELISA using the HT PARP in vivo PD Assay II Kit [4520-096-K] from R&D Systems. The remaining mice were measured twice weekly in three dimensions using Vernier calipers and the volume estimated using the formula ( $\text{width} \times \text{length} \times \text{depth} \times 0.524 \text{ mm}^3$ ). In the BL6 models, 4434 tumours were harvested from 3 mice from each group, 3 days post treatment and RNA was extracted (see Gene expression analysis using Nanostring below). No toxicity or weight loss was seen in any of the treated mice. Animals were judged to have failed treatment if tumor diameter approached the size limit of 15 mm in one of three dimensions, these limits were adhered to in all experiments. Tumours were measured twice-weekly. The humane end-point was euthanasia by neck dislocation due to moribund status, determined by weight loss of 18% or more compared with maximum weight measured, inability to reach food or water, breathing difficulties, anorexia, dehydration, marked piloerection, hunched intermittently, lethargy and subdued. The Kaplan–Meier survival curves were compared using the

log-rank (Mantel–Cox) test using Prism Software (GraphPad). Cured mice were rechallenged on the other flank with  $4 \times 10^6$  4434 cells and tumour growth monitored.

### Gene expression analysis using Nanostring (mouse Immune Profile)

Excised 4434 tumours following treatment (as above) were lysed in homogenization tubes (Thermo Fisher Scientific) containing buffer RLT (79126, Qiagen) using Precellys 24 homogenizer. RNA was then isolated using RNeasy Plus Mini Kit (74134, Qiagen) according to the manufacturer's instructions. RNA concentration was measured using Qubit Fluorometer system and Qubit RNA BR Assay Kit (ThermoFisher Scientific), and 96 ng of RNA was used in the nCounter Mouse Immunology Panel (Nanostring Technologies). Normalization, differential expression, geneset analysis and cell type scoring were performed using NanoString nSolver V.4.0 advanced analysis software. Data presentation used Rstudio V.1.4.1103, R V.4.1, ggplot2 and Complex Heatmap packages.

### Immune profiling of tumours

4434 cells were established in female BL6 immunocompetent mice by subcutaneous injection at  $4 \times 10^6$  cells. Tumours were allowed to grow to 6–8 mm before mice were allocated treatment groups stratified by tumour size. Tumours were harvested and weighed on Day 11, and dissociated (5 mice per group) mechanically using scissors and enzymatically digested in RPMI containing 0.5 mg/mL Collagenase type I-S (Sigma-Aldrich), 0.4 mg/mL Dispase II protease (Sigma-Aldrich), 0.2 mg/mL DNase I (Roche) and 4% Trypsin (0.25% in Tris Saline) for 30 min at 37 °C. Following digestion, samples were passed through a 70 µm cell strainer and washed with 10% FCS RPMI supplemented with 5 mM EDTA. Samples were centrifuged at  $300 \times g$ , for 5 min at 4 °C, and transferred into a V-well 96-well plate. Samples were stained in FACS buffer (PBS + 5% FCS) for 30 min on ice and protected from light, with extracellular antibodies. Cells were then washed in FACS buffer, permeabilized and stained with intracellular antibodies (refer to Supplementary Table 4). Samples were then washed and fixed (1–2% PFA) prior to analysis of tumour-infiltrating lymphocytes by flow cytometry. Tumours were weighed on collection and 123 count eBeads counting beads were added when running the analysis to calculate cells per mg of tumour. Data was collected using FACS DIVA 8.0.1 Version 9.3.1 (build 2021\_11\_30\_11\_38), and analysed using FlowJo version 10.10.0.

### Bliss Independence Analysis

Synergy interactions between different treatments were tested by standard mathematical analyses of data from MTT or SRB assays. Specifically, the presence (or absence) of synergy was quantified by Bliss Independence Analysis<sup>56–59</sup> described by the formulae  $E_{AB} = EA + EB - EA \cdot EB$  and  $\Delta E = E_{OBS} - E_{IND}$  where: EA and EB are the fractional effect of factors A and B, respectively; EIND is the expected effect of an independent combination of factors; E OBS is the observed effect of the combination. If  $\Delta E$  and its 95% confidence interval (CI) are  $>0$  synergy has been observed. If  $\Delta E$  and its 95% CI are  $<0$  antagonism has been observed. If  $\Delta E$  and its 95% CI contain 0 then the combination is independent. All plots were generated using Prism GraphPad software.

### Statistical analysis

Comparisons between groups were done using the Student's 't' test or ANOVA tests. Survival curves were estimated using the Kaplan–Meier method, and significance was assessed using the log-rank test.  $P$  values  $<0.05$  were considered to be statistically significant (\*,  $P < 0.05$ ; \*\*,  $P < 0.01$ ; \*\*\*,  $P < 0.005$ ).

### Reporting summary

Further information on research design is available in the Nature Portfolio Reporting Summary linked to this article.

### Data availability

All data are included in the Supplementary Information or available from the authors, as are unique reagents used in this Article. The raw numbers for charts and graphs are available in the Source Data file whenever possible. Proteomic data files have been uploaded to PRIDE repository<sup>55</sup> under project accession [PXD047621](https://doi.org/10.1038/s41467-025-61297-w). Source data are provided with this paper.

### References

- Kim, S. G. et al. Phase II trial of pexa-vec (*pexastimogene devacir-epvec*; JX-594), an oncolytic and immunotherapeutic vaccinia virus, in patients with metastatic, refractory renal cell carcinoma (RCC). *J. Clin. Oncol.* **36** (2018). Meeting Abstract: 2013 ASCO Annual Meeting.
- Cui, C. L. et al. OrienX010 oncolytic viral therapy in phase Ic trial of intralesional injection in liver metastases among patients with stage IV melanoma after standard treatment. *J. Clin. Oncol.* **35**, e21013 (2017).
- Andtbacka, R. H. et al. Talimogene laherparepvec improves durable response rate in patients with advanced melanoma. *J. Clin. Oncol.* **33**, 2780–2788 [https://doi.org/10.1200/JCO.2017.35.15\\_suppl.e21013](https://doi.org/10.1200/JCO.2017.35.15_suppl.e21013) (2015).
- Gollamudi, R. et al. Intravenous administration of Reolysin, a live replication competent RNA virus is safe in patients with advanced solid tumors. *Invest. N. Drugs* **28**, 641–649 (2010).
- Pecora, A. L. et al. Phase I trial of intravenous administration of PV701, an oncolytic virus, in patients with advanced solid cancers. *J. Clin. Oncol.* **20**, 2251–2266 (2002).
- Chesney, J. A. et al. Randomized, double-blind, placebo-controlled, global phase III Trial of talimogene laherparepvec combined with pembrolizumab for advanced melanoma. *J. Clin. Oncol.* **41**, 528–540 (2023).
- Dummer, R. et al. Neoadjuvant talimogene laherparepvec plus surgery versus surgery alone for resectable stage IIIB–IVM1a melanoma: a randomized, open-label, phase 2 trial. *Nat. Med.* **27**, 1789–1796 (2021).
- Harrington, K. J. et al. Talimogene laherparepvec and pembrolizumab in recurrent or metastatic squamous cell carcinoma of the head and neck (MASTERKEY-232): a multicenter, phase 1b study. *Clin. Cancer Res.* **26**, 5153–5161 (2020).
- Karapanagiotou, E. M. et al. Phase I/II trial of carboplatin and paclitaxel chemotherapy in combination with intravenous oncolytic reovirus in patients with advanced malignancies. *Clin. Cancer Res.* **18**, 2080–2089 (2012).
- Lolkema, M. P. et al. A phase I study of the combination of intravenous reovirus type 3 Dearing and gemcitabine in patients with advanced cancer. *Clin. Cancer Res.* **17**, 581–588 (2011).
- Comins, C. et al. REO-10: a phase I study of intravenous reovirus and docetaxel in patients with advanced cancer. *Clin. Cancer Res.* **16**, 5564–5572 (2010).
- Harrington, K. J. et al. Phase I/II study of oncolytic HSV GM-CSF in combination with radiotherapy and cisplatin in untreated stage III/IV squamous cell cancer of the head and neck. *Clin. Cancer Res.* **16**, 4005–4015 (2010).
- Harrington, K. J. et al. Two-stage phase I dose-escalation study of intratumoral reovirus type 3 dearing and palliative radiotherapy in patients with advanced cancers. *Clin. Cancer Res.* **16**, 3067–3077 (2010).
- Tung, N. & Garber, J. E. PARP inhibition in breast cancer: progress made and future hopes. *NPJ Breast Cancer* **8**, 47 (2022).

15. Pettitt, S. J. & Lord, C. J. PARP inhibitors and breast cancer: highlights and hang-ups. *Expert Rev. Precis. Med. Drug Dev.* **3**, 83–94 (2018).
16. Evans, T. & Matulonis, U. PARP inhibitors in ovarian cancer: evidence, experience and clinical potential. *Ther. Adv. Med. Oncol.* **9**, 253–267 (2017).
17. Farmer, H. et al. Targeting the DNA repair defect in mutant cells as a therapeutic strategy. *Nature* **434**, 917–921 (2005).
18. Bryant, H. E. et al. Specific killing of BRCA2-deficient tumours with inhibitors of poly(ADP-ribose) polymerase. *Nature* **434**, 913–917 (2005).
19. Huang, R. & Zhou, P. K. DNA damage repair: historical perspectives, mechanistic pathways and clinical translation for targeted cancer therapy. *Signal Transduct. Target Ther.* **6**, 254 (2021).
20. van der Noll, R. et al. Phase I study of intermittent olaparib capsule or tablet dosing in combination with carboplatin and paclitaxel (part 2). *Invest. N. Drugs* **38**, 1096–1107 (2020).
21. Grady, S. L. et al. Herpes simplex virus 1 infection activates poly(ADP-ribose) polymerase and triggers the degradation of poly(ADP-ribose) glycohydrolase. *J. Virol.* **86**, 8259–8268 (2012).
22. Passaro, C. et al. PARP inhibitor olaparib increases the oncolytic activity of dl922-947 in vitro and in vivo model of anaplastic thyroid carcinoma. *Mol. Oncol.* **9**, 78–92 (2015).
23. Shen, Y. et al. BMN 673, a novel and highly potent PARP1/2 inhibitor for the treatment of human cancers with DNA repair deficiency. *Clin. Cancer Res.* **19**, 5003–5015 (2013).
24. Pettitt, S. J. et al. Genome-wide and high-density CRISPR-Cas9 screens identify point mutations in PARP1 causing PARP inhibitor resistance. *Nat. Commun.* **9**, 1849 (2018).
25. Roulstone, V. et al. BRAF- and MEK-targeted small molecule inhibitors exert enhanced antimelanoma effects in combination with oncolytic reovirus through ER stress. *Mol. Ther.* **23**, 931–942 (2015).
26. Clarke, P. et al. Mechanisms of reovirus-induced cell death and tissue injury: role of apoptosis and virus-induced perturbation of host-cell signaling and transcription factor activation. *Viral Immunol.* **18**, 89–115 (2005).
27. Clarke, P. et al. Mechanisms of apoptosis during reovirus infection. *Curr. Top. Microbiol. Immunol.* **289**, 1–24 (2005).
28. Pennarun, B. et al. Playing the DISC: turning on TRAIL death receptor-mediated apoptosis in cancer. *Biochim. Biophys. Acta* **1805**, 123–140 (2010).
29. Thorburn, A. Death receptor-induced cell killing. *Cell Signal* **16**, 139–144 (2004).
30. Henry, C. M. & Martin, S. J. Caspase-8 Acts in a non-enzymatic role as a scaffold for assembly of a pro-inflammatory “FADDosome” complex upon TRAIL stimulation. *Mol. Cell* **65**, 715–729 e5 (2017).
31. Butera, F. et al. Actin networks modulate heterogeneous NF-kappaB dynamics in response to TNFalpha. *Elife* **13**, e86042 (2024).
32. Murai, J. et al. Stereospecific PARP trapping by BMN 673 and comparison with olaparib and rucaparib. *Mol. Cancer Ther.* **13**, 433–443 (2014).
33. Murai, J. et al. Trapping of PARP1 and PARP2 by Clinical PARP Inhibitors. *Cancer Res.* **72**, 5588–5599 (2012).
34. Yuan, K. et al. PARP-1 regulates resistance of pancreatic cancer to TRAIL therapy. *Clin. Cancer Res.* **19**, 4750–4759 (2013).
35. Cullen, S. P. et al. Fas/CD95-induced chemokines can serve as “Find-Me” signals for apoptotic cells. *Mol. Cell* **49**, 1034–1048 (2013).
36. Zhou, B. et al. RIG-I promotes cell death in hepatocellular carcinoma by inducing M1 polarization of perineal macrophages through the RIG-I/MAVS/NF-kappaB pathway. *Onco. Targets Ther.* **13**, 8783–8794 (2020).
37. Wang, H. et al. Synergistic lethality between PARP-trapping and alantolactone-induced oxidative DNA damage in homologous recombination-proficient cancer cells. *Oncogene* **39**, 2905–2920 (2020).
38. Hopkins, T. A. et al. Mechanistic dissection of PARP1 trapping and the impact on in vivo tolerability and efficacy of PARP inhibitors. *Mol. Cancer Res.* **13**, 1465–1477 (2015).
39. Hammerich, L. et al. Systemic clinical tumor regressions and potentiation of PD1 blockade with in situ vaccination. *Nat. Med.* **25**, 814–824 (2019).
40. Marquez-Rodas, I. et al. Intratumoral nanoplexed poly I:C BO-112 in combination with systemic anti-PD-1 for patients with anti-PD-1-refractory tumors. *Sci. Transl. Med.* **12**, eabb0391 (2020).
41. Moreno, V. et al. Treatment with a retinoic acid-inducible gene I (RIG-I) agonist as monotherapy and in combination with pembrolizumab in patients with advanced solid tumors: results from two phase 1 studies. *Cancer Immunol. Immunother.* **71**, 2985–2998 (2022).
42. Dhomen, N. et al. Oncogenic Braf induces melanocyte senescence and melanoma in mice. *Cancer Cell* **15**, 294–303 (2009).
43. Iorns, E. et al. Identification of CDK10 as an important determinant of resistance to endocrine therapy for breast cancer. *Cancer Cell* **13**, 91–104 (2008).
44. Iorns, E. et al. Utilizing RNA interference to enhance cancer drug discovery. *Nat. Rev. Drug Discov.* **6**, 556–568 (2007).
45. Twigger, K. et al. Enhanced in vitro and in vivo cytotoxicity of combined reovirus and radiotherapy. *Clin. Cancer Res.* **14**, 912–923 (2008).
46. Geissmann, Q. OpenCFU, a new free and open-source software to count cell colonies and other circular objects. *PLoS ONE* **8**, e54072 (2013).
47. Gyori, B. M. et al. OpenComet: an automated tool for comet assay image analysis. *Redox Biol.* **2**, 457–465 (2014).
48. Smith, H. G. et al. RIPK1-mediated immunogenic cell death promotes anti-tumour immunity against soft-tissue sarcoma. *EMBO Mol. Med.* **12**, e10979 (2020).
49. Feltham, R. et al. Mind bomb regulates cell death during TNF signaling by suppressing RIPK1’s cytotoxic potential. *Cell Rep.* **23**, 470–484 (2018).
50. Jaco, I. et al. MK2 phosphorylates RIPK1 to prevent TNF-induced cell death. *Mol. Cell* **66**, 698–710 e5 (2017).
51. Frankish, A. et al. GENCODE reference annotation for the human and mouse genomes. *Nucleic Acids Res.* **47**, D766–D773 (2019).
52. Nakagawa, S. & Takahashi, M. U. gVE: a genome-based endogenous viral element database provides comprehensive viral protein-coding sequences in mammalian genomes. *Database (Oxf.)* **2016**, baw087 (2016).
53. Kall, L. et al. Semi-supervised learning for peptide identification from shotgun proteomics datasets. *Nat. Methods* **4**, 923–925 (2007).
54. Tyanova, S. et al. The Perseus computational platform for comprehensive analysis of (prote)omics data. *Nat. Methods* **13**, 731–740 (2016).
55. Perez-Riverol, Y. et al. The PRIDE database resources in 2022: a hub for mass spectrometry-based proteomics evidences. *Nucleic Acids Res.* **50**, D543–D552 (2022).
56. Mansfield, D. et al. Oncolytic Vaccinia virus and radiotherapy in head and neck cancer. *Oral. Oncol.* **49**, 108–118 (2013).
57. Buck, E. et al. Rapamycin synergizes with the epidermal growth factor receptor inhibitor erlotinib in non-small-cell lung, pancreatic, colon, and breast tumors. *Mol. Cancer Ther.* **5**, 2676–2684 (2006).
58. Greco, W. R., Bravo, G. & Parsons, J. C. The search for synergy: a critical review from a response surface perspective. *Pharm. Rev.* **47**, 331–385 (1995).
59. Bliss, C. I. The calculation of microbial assays. *Bacteriol. Rev.* **20**, 243–258 (1956).

## Acknowledgements

We thank Oncolytics Biotech for providing reovirus and Harriet Whittock for all her help with in vivo work produced for this study. Research described in this manuscript is funded by CRUK programme (grant number CRM183X, AM). Kevin Harrington is supported by the RM/ICR NIHR Biomedical Research Centre.

## Author contributions

J.K.C., V.R., C.J.L., K.J.H. and A.M. contributed to the conception and design of the research as well as in writing the manuscript. J.K.C., V.R., J.W., F.B., A.L., R.E., G.B., M.D., V.J. and D.K. performed the experiments and acquired data. M.M., D.K., S.P., T.T., S.F., E.P., A.W., C.C.W.H., E.A., M.P., A.R., J.C., C.B. and P.M. contributed to the analysis and interpretation of the data. J.W., R.E., M.M. and C.J.D. provided support for bioinformatics analysis. All authors read and approved the final manuscript.

## Competing interests

The authors declare no competing interests.

## Additional information

**Supplementary information** The online version contains supplementary material available at <https://doi.org/10.1038/s41467-025-61297-w>.

**Correspondence** and requests for materials should be addressed to Joan Kyula-Currie.

**Peer review information** *Nature Communications* thanks George Ansstas, Ishani Banik and Samuel Rabkin for their contribution to the peer review of this work. A peer review file is available.

**Reprints and permissions information** is available at <http://www.nature.com/reprints>

**Publisher's note** Springer Nature remains neutral with regard to jurisdictional claims in published maps and institutional affiliations.

**Open Access** This article is licensed under a Creative Commons Attribution-NonCommercial-NoDerivatives 4.0 International License, which permits any non-commercial use, sharing, distribution and reproduction in any medium or format, as long as you give appropriate credit to the original author(s) and the source, provide a link to the Creative Commons licence, and indicate if you modified the licensed material. You do not have permission under this licence to share adapted material derived from this article or parts of it. The images or other third party material in this article are included in the article's Creative Commons licence, unless indicated otherwise in a credit line to the material. If material is not included in the article's Creative Commons licence and your intended use is not permitted by statutory regulation or exceeds the permitted use, you will need to obtain permission directly from the copyright holder. To view a copy of this licence, visit <http://creativecommons.org/licenses/by-nc-nd/4.0/>.

© The Author(s) 2025